POLITECNICO
MILANO 1863

SCUOLA DI INGEGNERIA INDUSTRIALE
E DELL'INFORMAZIONE

Neutronic study for GENeuSIS, a test facility for critical components of the ITER fusion reactor

Tesi magistrale in
Nuclear Engineering - Ingegneria Nucleare

Author: **Pier Giorgio Marchetti**

Student ID: 10765770
Advisor: Prof. Andrea Pola
Tutor: Rosaria Villari, Fabio Moro, Andrea Colangeli, Simone Noce
Academic Year: 2024-2025

Abstract

This thesis presents a neutronic study supporting the development and characterization of the GENeuSIS (General Experimental Neutron System Irradiation Station) test facility, designed to reproduce ITER-relevant radiation environments for diagnostics and electronic component testing. The system is optimized to emulate the neutron energy spectrum of the ITER Equatorial Port Cell using a 14 MeV D–T neutron source at the Frascati Neutron Generator (FNG).

Monte Carlo simulations performed with MCNP were used to characterize neutron and photon fields inside the irradiation cavity, assessing, where present, their irregularities and anisotropies. Particular attention was devoted to spatial and angular distributions, as well as spectral variations within the cavity. The results demonstrate that GENeuSIS-II successfully reproduces the target ITER spectrum with good spectral agreement and flux intensity, although knowledge of the flux distribution within the cavity will be required to optimize the experiments.

Keywords: Monte Carlo simulation, fusion neutronics, radiation effects on electronics, ITER Equatorial Port, GENeuSIS

Abstract in lingua italiana

Questa tesi presenta uno studio neutronico a supporto dello sviluppo e della caratterizzazione dell'assemblaggio sperimentale GENeuSIS (General Experimental Neutron System Irradiation Station), progettata per riprodurre ambienti radioattivi rilevanti per il reattore ITER, destinati alla qualificazione di diagnostiche e componenti elettronici. L'apparato sperimentale è stato ottimizzato per emulare lo spettro energetico neutronico della Equatorial Port Cell di ITER utilizzando una sorgente neutronica D–T da 14 MeV, disponibile presso il Frascati Neutron Generator (FNG).
Sono state impiegate simulazioni Monte Carlo eseguite con MCNP per caratterizzare i campi neutronici e fotonici all'interno della cavità di irraggiamento, valutandone, ove presenti, eventuali irregolarità e anisotropie. Particolare attenzione è stata dedicata alle distribuzioni spaziali e angolari, nonché alle variazioni spettrali all'interno della cavità.
I risultati dimostrano che GENeuSIS-II è in grado di riprodurre lo spettro target di ITER con buon accordo spettrale e adeguata intensità di flusso; tuttavia, una conoscenza dettagliata della distribuzione del flusso all'interno della cavità sarà necessaria per ottimizzare le future campagne sperimentali.

Parole chiave: simulazione Monte Carlo, neutronica da fusione, effetti delle radiazioni sull'elettronica, ITER porta equatoriale, GENeuSIS

Contents

Introduction

For the past 80 years nuclear fusion has been considered a promising source of nearly unlimited emissions-free energy for the future of mankind. It would have many advantages compared to nuclear fission: it has intrinsic safety characteristics, minimal long lived radioactive waste production, low carbon emissions and it could be capable of meeting a significant portion of the global energy demand.

It boasts a theoretically almost unlimited fuel supply since it relies on the fusion reaction of deuterium and tritium: the former can be extracted from seawater, where it is abundant, and the latter can be produced inside the reactor itself using special lithium blankets that are now being developed and tested. This would allow for a self sustaining fuel cycle.

It is a safe technology because it completely erases the possibility of a reactor meltdown, as the reactor requires extremely precise operating conditions to operate and any disruption would stop the reaction. It would also remove the risk of nuclear proliferation since its waste products cannot be used to make nuclear bombs.

For all of the reasons above fusion reactors have been very attractive to researchers and a multitude of facilities have been built all over the world to investigate and address the many challenges that have so far stopped this new technology from being commercially viable [1][2][3].

These challenges include: creating a stable plasma where the fusion reactions can take place in a self sustaining manner, the development of materials capable of sustaining the enormous thermal loads and neutron fluxes and the reduction of radiation induced damage on sensible components.

An example of those research facilities is the International Thermonuclear Experimental Reactor (ITER) [4], a multinational megaproject that aims to address many of the issues related to plasma stability and fusion technology development [5]. Not only is this reactor one of the most complex machines ever built by mankind, but it also threads into uncharted territory when it comes to the collateral effects that a prolonged fusion reaction can have on its surroundings.

In this context lies the goal of GENeuSIS: to further our understanding of the effects that

the radiation field of a large tokamak like ITER can have on the electronic components around it.
The GENeuSIS assembly is designed to be installed in front of a DT neutron generator and to act as an experimental neutron moderation and irradiation system. Its purpose is to reproduce, within a dedicated irradiation cavity, the neutron energy spectra expected at specific locations in ITER, particularly in the diagnostic ports where radiation-sensitive electronics and instrumentation are installed.
The main objectives of the GENeuSIS system include: calibration of neutron diagnostics, testing critical diagnostics tools and performing single event effects (SEE) studies on electronic components. To meet these objectives, GENeuSIS has been designed according to the following key requirements:

- Modular;
- Transportable;
- Flexible;
- Customizable;
- Multi-purpose;
- Based on combinations of common materials.

The modular design enables easy assembly and disassembly, allowing the system to be deployed not only at the reference DT neutron generator but also at other similar neutron facilities. The irradiation spectra can be tailored by replacing or rearranging individual moderation layers, making it possible to reproduce different neutron energy distributions.
The main objective of this Master's thesis is to support the characterization of the neutron and gamma radiation fields within the irradiation cavity of the GENEuSIS device, in preparation for the planning of an initial experimental campaign to be carried out at the DT neutron source FNG (Frascati Neutron Generator) at the ENEA laboratories in Frascati [6].
The first experimental tests will be on Static Random Access Memories (SRAMs) placed inside the device's cavity.

1 | Nuclear fusion and neutronics

1.1. Fusion reactions

There are two possible ways to obtain a large amount of energy from nuclear reactions: fission and fusion. The energetic convenience of these processes can be understood by considering the binding energy per nucleon as a function of the mass number, as shown in Figure 1.1: nuclei up to Fe^{56} release energy when fused together and nuclei after said iron isotope release it when split (fissioned) [7].

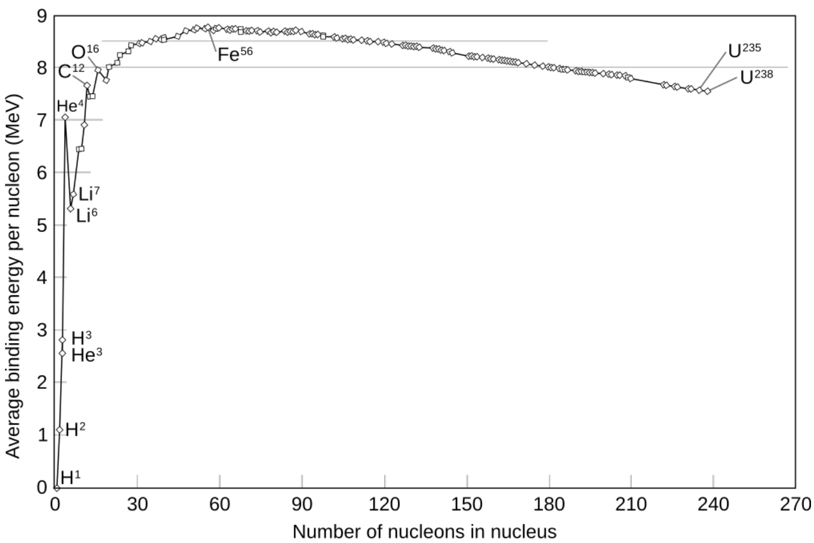

Figure 1.1: The average nucleon binding energy per nucleon [8].

Among the various fusion reactions that can, in principle, be exploited for energy production, the ones that have attracted the greatest interest are the Deuterium–Deuterium (D–D) and Deuterium–Tritium (D–T) reactions. Both deuterium and tritium are isotopes of hydrogen, making them suitable candidates for fusion due to their relatively low Coulomb repulsion compared to heavier nuclei. The deuterium–deuterium reaction can occur through two main branches:

$$D + D \rightarrow {}^{3}He\ (0.82\,MeV) + n\ (2.45\,MeV) \tag{1.1}$$

$$D + D \rightarrow T\ (1.01\,MeV) + p\ (3.02\,MeV) \tag{1.2}$$

Each branch releases a total energy of approximately 3–4 MeV. Although the D–D reaction has the advantage of using only deuterium, which is naturally abundant, it presents significant challenges due to its relatively low reaction cross section, requiring higher plasma temperatures to achieve a net energy gain [9].
The D-T reaction on the other hand generates a 3.4 MeV alpha particle and a 14.1 MeV neutron.

$$D + T \rightarrow {}^{4}He\ (3.5\,MeV) + n\ (14.1\,MeV) \tag{1.3}$$

The high energy of the neutron, while beneficial for the energy output of the reactor, combined with the fact that the neutron is a neutral particle and therefore can't be confined in the plasma, makes it very hard to stop. The side effects are that it's very challenging to harvest the energy carried by the neutron, since a significant amount of shielding is required to stop it completely, and that the escaped neutron can deal significant damage to the materials that form the reactor itself, like structural steels or the superconducting magnetic coils.
The alpha particle, meanwhile, being electrically charged, remains confined within the plasma and contributes to its self heating, a crucial aspect of sustaining the fusion process.

1.2. Neutrons interaction with matter

Neutrons are neutral particles, which means that they mainly interact with matter by colliding directly with the nuclei of atoms.
Any nuclear reaction has an associated microscopic cross section σ expressed in barns ($1\ \text{barn} = 10^{-24}\,\text{cm}^2$) that is related to the probability of that reaction occurring through the following equation:

$$R = N\,\phi\sigma$$

where R is the reaction rate expressed in reactions per seconds per unit volume, ϕ is the total neutron flux expressed in n/cm^2/s and N is the atomic density expressed in atoms/cm^3.

Most cross sections are strongly dependent on the energy and follow a similar trend. At low energies, in the so called 1/v region, an inverse relationship can be seen between the velocity of the incident particle and the cross section. At intermediate energies, in the resonance region, there are sharp irregular peaks while at high energies, the fast region describes interactions with relatively smooth energy dependence.

Figure 1.2 illustrates the cross sections dependence on incident particle's energy for several neutron interactions relevant for fusion neutronics [10].

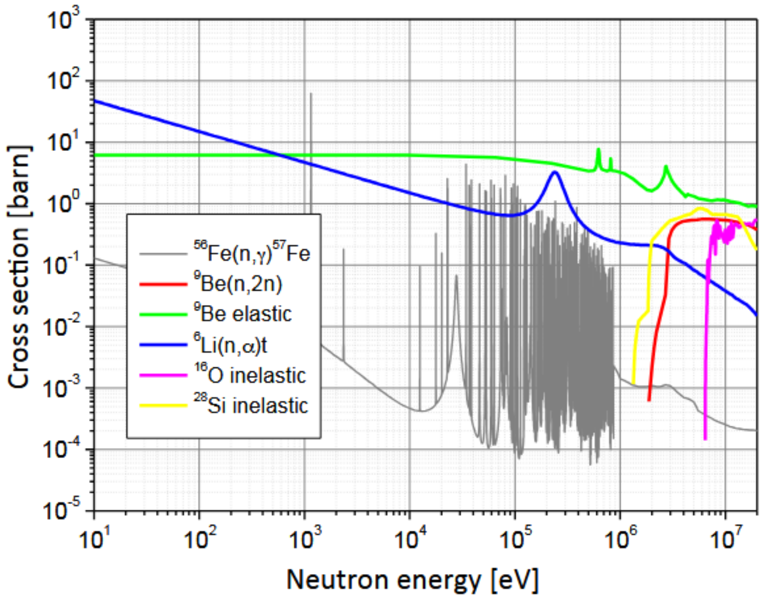

Figure 1.2: Neutron cross section data for fundamental reactions in nuclear fusion [10].

These interactions are classified into two main types: scattering and absorption. The first leads to a change in the neutron's trajectory and kinetic energy while the latter causes its complete removal from the system.

The total cross section, denoted as σ_t, quantifies the probability that any interaction will happen when a neutron encounters a nucleus. It can be written as the sum of the partial cross sections:

$$\sigma_t = \sigma_s + \sigma_a \tag{1.4}$$

where σ_s is the scattering cross section and σ_a is the absorption cross section. A brief explanation of the main types of neutron interactions with matter is provided below:

- **Elastic scattering**: the neutron bounces off the nuclei, transferring some of its energy to it. The total kinetic energy of the system doesn't change.
  If a neutron with kinetic energy E collides with a nucleus of atomic mass A, the average energy loss per collision is given by:

$$E_{\text{avg}} \approx \frac{2EA}{(A+1)^2} \tag{1.5}$$

  Lighter nuclei like hydrogen are excellent at slowing down neutrons (i.e they are good moderators), since their low mass allows them to gain a good chunk of the neutron's energy as shown in equation 1.5. Moderators are crucial in bringing neutrons from the fast region to the thermal one, since the latter is usually where the cross sections are the highest. In general, after n elastic collisions, the neutron's energy is expected to change from an initial energy E_0 to:

$$E_n = E_0 \left(\frac{A-1}{A+1} \right)^n \tag{1.6}$$

  Consequently, the average number of collisions required to reduce the neutron's energy to E_n is:

$$n = \frac{\log(E_n/E_0)}{\log\left(\frac{A-1}{A+1}\right)} \tag{1.7}$$

  For example to slow down a 2 MeV neutron to 0.025 eV (Thermal energy) at least 27 collisions are required [11][12][13].

- **Inelastic scattering**: the process is similar to the elastic case with the difference that the kinetic energy is not conserved, as part of it is used to excite the nuclei to a higher energy state. It occurs when a neutron has sufficient kinetic energy, typically in the range of 0.1 to 1 MeV, and the target nucleus has a medium mass.
  The energy transferred to the nucleus during this process depends not only on its mass but also the structure of its energy levels.
  The target nucleus eventually emits one or more photons, which can carry significant energy. Therefore inelastic scattering can be an effective mechanism for reducing the energy of neutrons in heavy nuclei such as iron or other structural metals.
  However this process isn't always possible: if the incoming neutron doesn't have enough energy to reach the first excited state of the nucleus the reaction cannot

occur. A notable example is the case of Hydrogen, an atom whose nucleus does not have excited states.

- **Absorption**: the neutron is absorbed by the nuclei. The resulting atom can either be a stable isotope or decay later, emitting one or more photons or other charged particles such as protons, deuterons and alpha particles. The nucleus may also emit additional neutrons. This type of reaction predominantly occurs when neutrons interact with heavy nuclei, producing two or more neutrons, whose energy can sometimes exceed that of the incoming neutron. This is the process exploited by nuclear fission to generate energy. As a result including materials that induce multiplication in a neutron shield is generally undesirable, since it may increase the neutron flux.
  In the field of nuclear fusion there are many detectors that exploit absorption reactions as the detection principle: since neutrons carry no electric charge they are difficult to detect, but if instead the neutron is first absorbed by a nucleus, which then emits a charged particle or gamma ray, detection becomes much easier.
  Common detector materials for low-energy neutrons include ^{3}He, ^{235}U, and ^{10}B, as they possess large absorption cross sections and efficiently produce charged particles upon neutron capture.

Materials that undergo neutron bombardment can either become radioactive and/or see their properties change [14][15].

1.2.1. Damage to electronics

In ITER, electronics responsible for control, diagnostics and safety are exposed to intense neutron and gamma radiation. Even temporary errors can disrupt machine operation, while permanent failures may cause costly damage or downtime. Reproducing ITER-like radiation conditions and studying the response of electronic components will enable more reliable designs and effective mitigation strategies. Electronics are susceptible to two kind of damage when exposed to a radiation field: soft errors, that are temporary and can be reset, and hard errors, that are permanent and might destroy the component itself.
Memories are particularly vulnerable to soft errors like Single Event Upsets (SEUs), where a particle strikes a memory element, causing a bit flip and corrupting the memory in the process. To be more precise a SEU occurs when a particle induces a sufficent amount of ionization in the off-state transistor of a cross-coupled inverters pair, the building block of modern SRAM memories [16][17].
As transistor dimensions continue to shrink, a single particle strike can effect multiple

bits, increasing the error rate, in what's called a Multiple Bits Upset (MBU). It must be noted that MBUs rate, depending on the memory architecture, can be strongly dependent on the orientation of the memory with respect to the striking particle [17].
Other types of memories like Complementary Metal-Oxide Semiconductor (CMOS) are more susceptible to hard errors like the ones caused by a Single-Event Latchups (SELs), which damage the bit by inducing a strong current that can become catastrophic if the component isn't reset quickly.
Other types of Single Event Effects include Single Event Functional Interrupts (SEFI), gate ruptures or burnouts. Thus knowledge of the nanostructure of electronic components and of the types of failures they can suffer is important to the goal of this thesis and of the GENeuSIS project, since it will allow for a more precise and efficient approach to the design of the experiments.

2 | Fusion technology

So far the two main technologies that have been employed to investigate fusion are Inertial Confinement Fusion (ICF) and Magnetic Confinement Fusion (MCF).

Inertial confinement is based on the fast compression of a fuel pellet using high power lasers or particle beams to achieve the extremely high temperatures and pressures required to achieve the fusion reaction. The drawback is that the reaction lasts for a fraction of a second before the pellet is depleted and needs to be reloaded. On the other hand magnetic confinement aims to sustain the reaction for longer periods of time by isolating the fuel from the reactor walls through magnetic fields.

Among these two technologies, the latter is the one that has gathered the most interest when it comes to designing reactors capable of producing a continuous stream of energy, which are the ones that commercial applications would require.

The goal of magnetic confinement is to heat up a plasma obtained from a gas mixture of deuterium and tritium until it reaches 150 million degrees Celsius. At these temperatures the kinetic energy of the particles is sufficient to overcome the Coulomb repulsion between positively charged nuclei, allowing fusion reactions to occur.

Here lies one of the biggest challenges faced by MCF: maintaining these extreme conditions while ensuring that the plasma remains stable for extended periods of time.

Since the 1950s a wide array of machines have been devised to confine plasmas using magnetic fields and their designs are still being improved upon today as computational capabilities and material sciences progress. The most notable MCF machine configurations include the Tokamak, the Stellarator, the Magnetic Mirror, the Field Reverse Configuration and the Z-pinch.

Each of these devices has its advantages and technical challenges. Ongoing research is currently attempting to improve their performance in terms of plasma stability, confinement time and energy efficiency [9][18].

2.1. The tokamak and the scaling solution

So far, the most successful design has been the Tokamak: it has achieved the highest temperature, the longest stable plasma and the highest triple product ever recorded. This last metric comes from the Lawson Criterion, a simple and powerful formula that, based on the main fusion reactor design parameters, can establish the conditions for achieving fusion ignition. The criterion states that fusion can occur if:

$$n\,T\,\tau_E \geq \frac{12}{E_{ch}}\frac{T^2}{\langle \sigma v \rangle} \tag{2.1}$$

where n is the plasma density, T is the temperature, τ_E is the confinement time, E_{ch} is the energy of the charged particle released by the reaction, σ is the fusion cross section, v is the relative velocity, and $\langle\ \rangle$ denotes an average over the Maxwellian velocity distribution at the temperature T.
For the D-T reaction the criterion shows a minimum at T=14 keV (1.62×10^8K), where:

$$n\,T\,\tau_E = 3 \times 10^{21} \mathrm{keV\,s\,m^{-3}} \tag{2.2}$$

It follows that, as long as the triple product is above this value, ignition can be achieved. JT-60, a tokamak, achieved a triple product of 1.53×10^{21} $\mathrm{keV\,s\,m^{-3}}$ in 2013.
These parameters also put a limit to the reactors currently in operation, since in a Tokamak the confinement time scales with the major radius of the reactor to the power of 1.3-1.5 [19]. On paper, scaling makes Tokamak great candidates for fusion power production, as building a bigger reactor improves its performance. This is the idea behind the ITER project.

2.2. ITER: The International Thermonuclear Experimental Reactor

ITER is currently one of the world's largest and most complex experiments for thermonuclear fusion applications. It's the product of a joint venture that includes the European Union, the United States, Russia and Japan, China, India, and Korea. Each partner contributes to the project realisation which is in progress in the south of France (site of Cadarache) and they share in the cost of project construction, operation and decommissioning, as well as, future experimental results and any intellectual property generated

by the project. Twenty years of collaborative research experiments are planned on the machine [4][5].
Its main goals are:

- Achieving a deuterium-tritium plasma where the fusion conditions are sustained mostly by the internal heating generated by the fusion reaction itself. This goal would be met if the reactor can reach Q=10 for a very short time and Q=1 for at least 10 minutes, where Q is defined as the ratio of the heat released by fusion and the heat that's introduced in the reactor to heat up the plasma. A reactor with Q>1 produces more heat than what it consumes, which is the basic requirement for power generation, although commercial plants will require a bare minimum of Q>4 since one needs to take into account conversion losses. For example the ITER reactor is expected to produce 500 MW of fusion power from 50 MW of input heating power.

- Contribute to the demonstration of the integrated operation of technologies for a fusion power plant. ITER will be a step up from today's smaller-scale experimental fusion devices and will demonstrate the feasibility of fusion power plants of the future. Scientists will be able to study plasmas under conditions similar to those expected in a future power plant and test technologies such as heating, control, diagnostics, cryogenics and remote maintenance.

- Test tritium breeding. In the later stages of ITER operation the facility is expected to demonstrate the feasibility of producing tritium from lithium (lithium isotope ^{6}Li) within the vacuum vessel, since the world's supply of tritium will not be sufficient to cover the needs of future power plants.

- Demonstrate the safety characteristics of a fusion device, as one of the primary goals of ITER operation is to demonstrate control of the plasma and fusion reactions with negligible consequences to the environment [2][20].

2.2.1. ITER's Components

To achieve magnetic confinement, which implies confining and stabilizing the plasma, ITER employs a complex system of superconducting coils designed to generate and control the magnetic fields. It's composed of 18 toroidal field coils, 6 poloidal field coils, 1 central solenoid and 18 correction coils. When these coils are all active they allow the plasma shape and position to be tuned in three dimensions.
The 18 toroidal field coils are approximately 17 meters tall and they are arranged symmetrically around the tokamak's vacuum vessel [10]. They are responsible for producing the toroidal magnetic field, which can go as high as 5.3 T at its core and provides the primary

mechanism for confinement by forcing the charged particles to follow helical trajectories along magnetic field lines.

The central solenoid, in conjunction with the poloidal field coils, is responsible for the induction and control of the plasma current, which in turn generates the poloidal magnetic field necessary to stop the confined particles from drifting away [21].

The correction coils are used to compensate for magnetic field asymmetries and to mitigate magnetohydrodynamic instabilities.

Under nominal operating conditions, this magnetic configuration is designed to confine a plasma with a volume of $837\,\mathrm{m}^3$, which would make ITER the largest tokamak ever constructed [4].

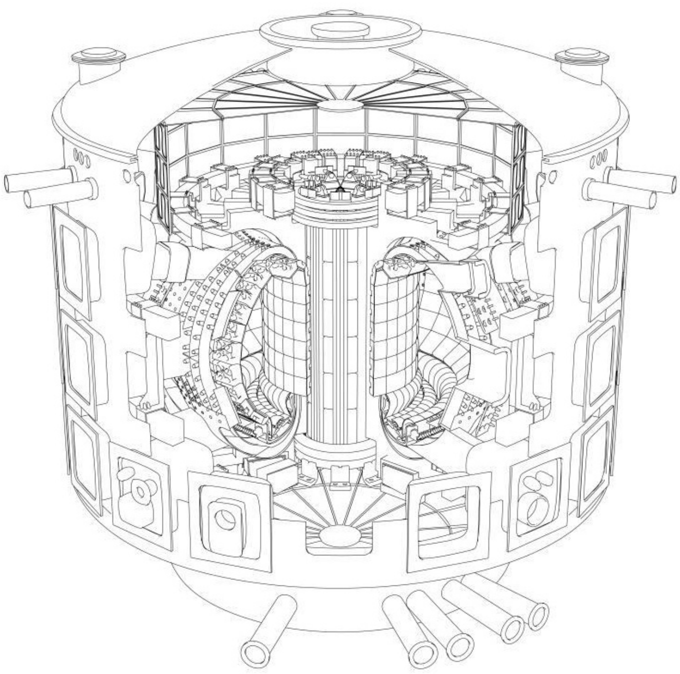

Figure 2.1: Vacuum vessel and cryostat [4].

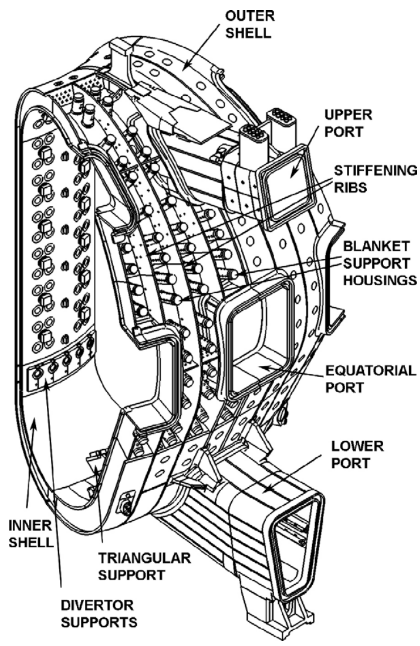

Figure 2.2: Cross section of the vacuum vessel [22].

These coils surround the vacuum vessel, which is the toroidal structure visible at the center of figure 2.1. The vacuum vessel is designed to withstand extreme neutron irradiation, electromagnetic stresses, thermal loads and vacuum, since it houses the magnetically confined plasma itself.

The inner surface of the vessel is lined with the blanket, a modular layer designed to shield radiation, protect the vacuum vessel from plasma transients and extract heat from the reactor. It's comprised of 440 individual modules, each consisting of a "first wall" panel made of tungsten, which is the plasma facing component that must resist extreme temperatures, followed by a 3 ton steel "shield block". Embedded within these modules

there are cooling channels necessary to keep everything cool enough not to melt under operation.
On the bottom of the vessel sits the divertor, which is one of the components that faces the highest temperatures (up to 3000°) and particle fluxes, since its functions are to extract heat and to clean the plasma from the helium ash produced by the fusion reaction. For this reason it will be made primarily of tungsten, due to its high melting point and low sputtering yield, and it will be cooled with water.
All of the components described so far are contained in the cryostat, the outermost shell visible in figure 2.1. It is the largest stainless steel high-vacuum pressure chamber ever built and it provides the high vacuum, 4.5 K environment for the ITER vacuum vessel and the superconducting magnets. To provide access to the diagnostics, cooling pipes and other utilities it has over 200 penetrations, some as large as 4 meters [4].

2.2.2. The Equatorial Port

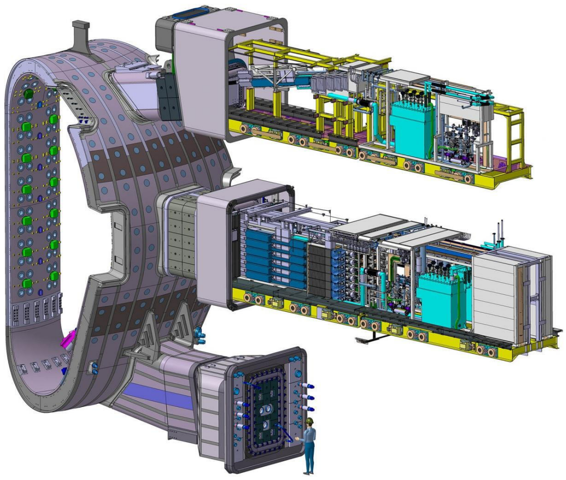

Figure 2.3: From the top: Upper Port, the Equatorial Port and the Lower port [4].

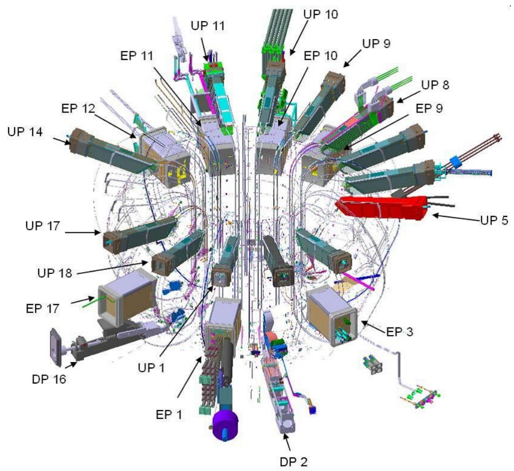

Figure 2.4: Schematic representation of the full diagnostic port system foreseen for ITER [4].

ITER houses a wide array of diagnostic systems to provide the researchers with the information required to control and optimize the operations performed within the reactor [23][24]. For this reason it houses 50 different types of diagnostic systems that can take measurements from the plasma, many of which are redundant to improve safety and accuracy. Measurements can be taken through the ports visible in figure 2.2 and 2.4, which are classified in Upper Ports, Equatorial Ports, and Lower Ports.

The diagnostic systems connect to these ports through a series of Port Plugs (PPs), which are are based on a standardized "box-type" construction (figure 2.5), with configurations adapted to the port level (upper, equatorial or lower). Inside the Port Plug assembly, the diagnostic components interface with a standardized Diagnostic Shield Module (DSM). Each upper port contains one DSM while each equatorial port has three (as visible in figure 2.5). Usually one to three different diagnostic systems can be integrated within a single DSM, depending on the technical requirements and spatial constraints.
In front of each DSM a Diagnostic First Wall (DFW) is installed as a plasma facing component, providing shielding and protection from direct plasma exposure [25].

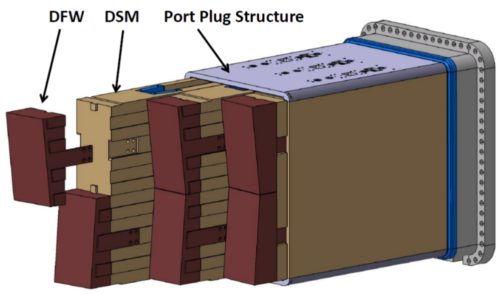

Figure 2.5: Port Plug [25].

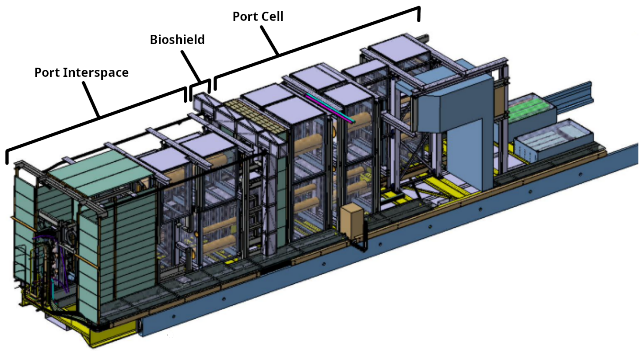

Figure 2.6: Port Interspace and Port Cell [26].

The Port Plugs are followed by a Port Interspace region and a thick biological shield, referred to as the bioshield, responsible for separating the high radiation environment of the tokamak from the areas accessible by the staff. That's because immediately behind the bioshield there is the Port Cell region (PC), which houses auxiliary diagnostic equipment that requires shielding.
A fundamental requirement is that all these port assemblies must be fully removable to allow remote handling and maintenance operations. To meet this requirement the port integration architecture relies on three main structural elements: the Port Plug Structure (PPS) in the in-vessel region, the Interspace Support Structure (ISS) and the Port Cell Support Structure (PCSS) in the ex-vessel region. The last two of these structures are equipped with rail systems, visible in figure 2.6, while the extraction of the Port Cell requires manual intervention.
The Upper Ports mainly host diagnostics devoted to global plasma monitoring and control, such as bolometry, visible and infrared imaging systems and vertical neutron cameras, providing poloidal views of the plasma and information on radiated power and plasma shape.

The Lower Ports, located close to the divertor region, are primarily dedicated to diagnostics related to plasma–wall interaction and divertor physics, including neutron flux monitors, spectroscopy and systems operating in the harshest radiation and thermal environments.
Equatorial Ports have a central role in neutron and gamma diagnostics, as they offer a direct radial line of sight to the plasma core and edge. In particular, the ITER Equatorial diagnostic port hosts several key neutron and radiation diagnostics and represents a reference configuration for GENeuSIS [25][27].
The neutron spectra adopted for both of the GENeuSIS is located in the ex-vessel region of ITER Equatorial Port 12 (EP#12): GENeuSIS-I was modeled after the spectrum of the Interspace region and GENeuSIS-II after the one of the Port Cell region.
To be more precise the reference spectra for GENeuSIS-II, the subject of this thesis, were taken from "workstation 5", labelled with the number 1 in figure 2.7.

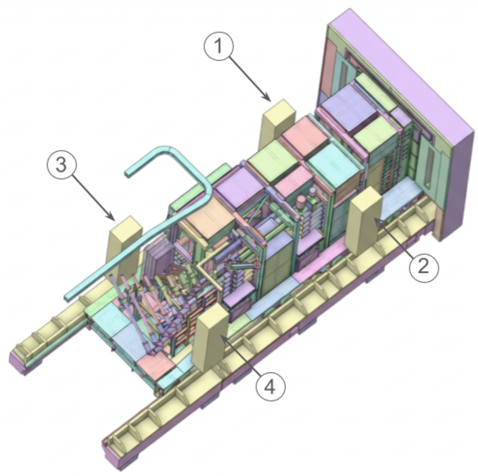

Figure 2.7: The four reference workstations [26].

These workstations are empty regions of space used as a reference to measure the energy spectrum in the Port Cell. The electronic components aren't located directly within them but around them, often with additional shielding. But because the ITER project is still in development and the components can be modified from year to year these workstations positions were chosen as a stable reference point [28].

2.3. FNG: The Frascati Neutron Generator

The Frascati Neutron Generator (FNG) is a neutron generator designed and built at the ENEA Energy Center of Frascati. It generates 14 MeV neutrons by accelerating

Deuterium Ions up to 300 keV and colliding them against a tritiated titanium target. It's capable of producing up to $5 \cdot 10^{11}$ n/s [6].
This neutron source is of paramount importance to the GENeuSIS experiment since it will be the one delivering the neutrons and all of the simulations performed in this study are based on it.

2.3.1. Technical breakdown

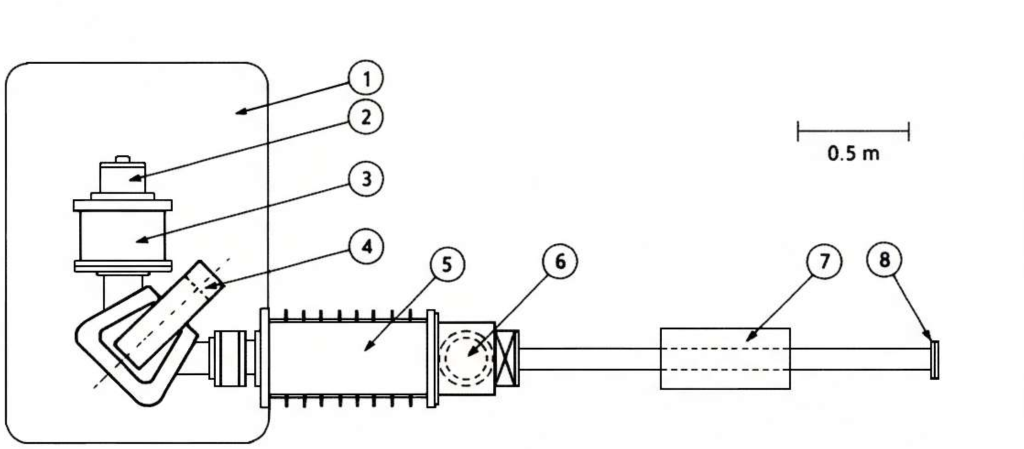

1	H.V. terminal	**3**	Extraction optics	**5**	Accelerating tube	**7**	Q-lens
2	Ion source	**4**	Bending magnet	**6**	Vacuum system	**8**	Target

Table 2.1: Top view of the main components [6].

A duoplasmatron ion source generates a beam of atomic and molecular hydrogen that gets subsequently filtered by a right angle bending magnet. This magnet produces a 1.6 T magnetic field and its purpose is to remove the molecular deuterium ions D_2^+ and D_3^+ as they increase the tritium sputtering, further decreasing the lifespan of the target.
The deuterium ions that pass are then accelerated up to 300 keV through the accelerating

Parameter	**D-T mode**	**D-D mode**
Max neutron yield	5×10^{11} n/s	1×10^{9} n/s
Max neutron flux (volume)	5×10^{9} n cm^{-2}s^{-1}	5×10^{7} n cm^{-2}s^{-1}
Max irradiation time per target	25 hours (one target, full power)	Continuous
Average utilization per year	> 150 hours/year	
Max achievable fluence	5×10^{15} n/cm^{2}	1×10^{13} n/cm^{2}

Table 2.2: Comparison of D-T and D-D operation modes. The max achievable fluence is intended on a 1 cm^3 sample

tube, where multiple series of resistor strings distribute the voltage uniformly.
The beam is then focused onto the target by the Q-lens, a series of three quadrupoles with a magnetic field of 0.15 T. The spot size is 15 mm. The target is comprised of a 4.4 µm thick layer of titanium that has been adsorbed with tritium, reaching a concentration of around 300 GBq, and placed in a copper cup. The latter, in conjunction with a closed loop water recirculation system, helps with cooling, since above 200°C the tritium starts to vaporize.
Due to sputtering, during the bombardment a substantial amount of tritium will be released from the target, which is why FNG is equipped with a Vacuum Exhaust Clean-up Unit (VECU)[6].
The fact that FNG works by accelerating deuterons at around 250 keV affects what would otherwise be a simple 14.1 MeV isotropic distribution.

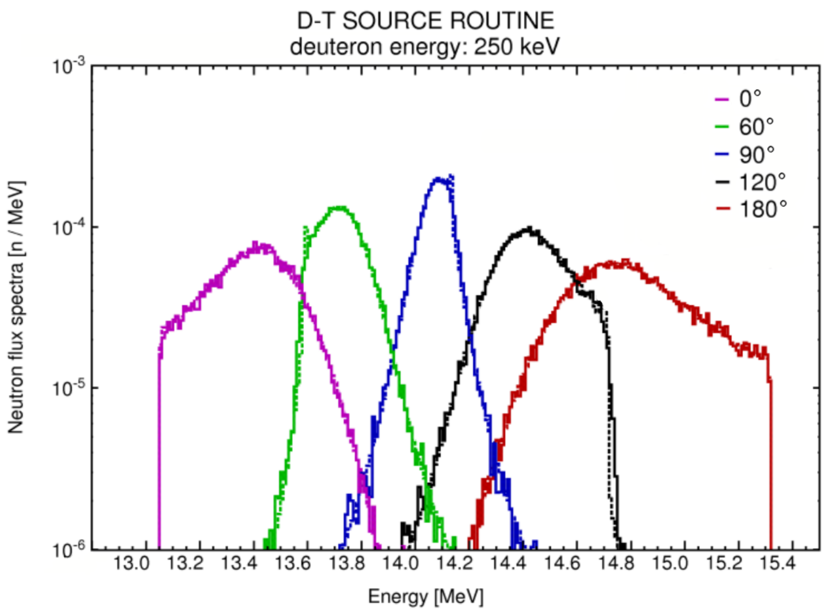

Figure 2.8: D-T neutron flux around FNG target obtained through MCNP. Continuos lines correspond to cell flux and the dotted ones to point detectors.

From an energy standpoint, the incident deuteron will contribute to the momentum balance of the reaction, resulting in an energy dependency on the emission angle θ visible in the graph from figure 2.8. The energy of the neutron E_n can be obtained through the equation:

$$E_n = \frac{1}{2} m_n V_{CM}^2 + \frac{m_\alpha}{m_\alpha + m_n}(Q + K) + V_{CM}\cos(\theta)\sqrt{2\mu(Q + K)} \tag{2.3}$$

where Q=17.9 MeV for the D-T reaction, K is the relative kinetic energy, V_{CM} is the velocity of the centre of mass of the reactants, θ is the neutron scattering angle with respect to the direction of the deuteron, m_α is the alpha particle's mass and m_n is the neutron's mass [29].

$$K = \frac{1}{2}\mu(v_d - v_t)^2 \qquad V_{\text{CM}} = \frac{m_d v_d + m_t v_t}{m_d + m_t} \qquad \mu = \frac{m_d m_t}{m_d + m_t}$$

3 | Monte Carlo methods

3.1. Introduction to Monte Carlo

Studying how a stream of particles, like neutrons, behaves inside a three dimensional geometry over time requires solving the Neutron Transport Equation, which is derived from the Boltzmann Equation. Obtaining an analytical solution is, in most realistic cases, impossible since the equation requires the user to know, at each time instant for each neutron, its 3 coordinates in space, its angular direction and its energy. And this is for a system comprised of billions of neutrons [30][31].
What's often done to tackle this issue is to adopt a series of assumptions that simplify the problem, like assuming that the neutron's energy can only take a value in a specific range or discretizing space, until the equation becomes solvable.
Another approach is using Monte Carlo methods. They follow each neutron from its source to its "death", using random numbers to simulate probabilistic events, like scattering and absorption, where the probability of one or more of these events occurring is given by the cross sections contained in the nuclear data. As more particle histories are simulated, the results become statistically significant and the relative estimated quantities are tallied. The code can also estimate the error relative to these tallied values and the more particle histories are run the lower these errors will be. To be more specific, the error follows a trend comparable to $1/\sqrt{N}$, where N is the number of neutron histories simulated.
What makes these type of calculations very convenient is visible in figure 3.1: as the complexity of the problem at hand increases, the time to solution increases almost linearly, compared to the analytical approach's exponential relationship. On the other hand Monte Carlo isn't the most efficient for simple geometries, due to the stochastic nature of the technique: a large number of particles will always be needed to obtain a statistically relevant solution [32][14][15][33].

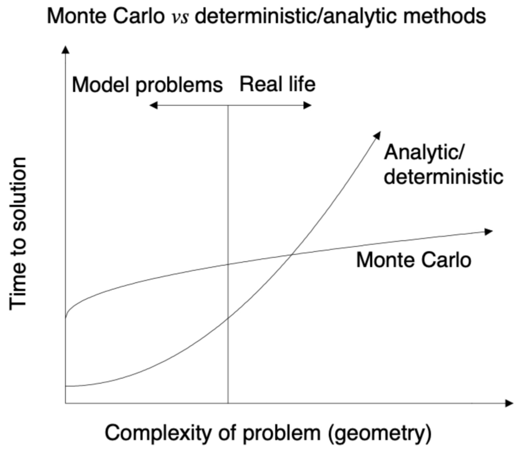

Figure 3.1: This graph shows how the more complex a model gets, the more appealing Monte Carlo methods become[26].

3.2. MCNP

The Monte Carlo N-particle Transport Code (MCNP) is a general-purpose Monte Carlo code that can be used for neutron, photon, electron, or coupled neutron/photon/electron transport, including the capability to calculate eigenvalues for critical systems. It was first conceived in 1947 by Stanislaw Ulam at Los Alamos National Laboratory and was executed on the world's first digital computer, the ENIAC, a year later.

Important features that make MCNP a versatile software are: a powerful general source, a criticality source, a set of variance reduction techniques, a flexible tally structure and a vast collection of cross-section data.

The types of tallies available, summarised in table 3.1, include: surface current and flux, volume flux (track length), point or ring detectors, particle heating, fission heating, pulse height tally for energy or charge deposition, mesh tallies and radiography tallies. All of these tools make MCNP the reference tool for the neutronic analyses in the frame of the ITER project, since it has been the subject of a large number of experimental and theoretical benchmarks.

In this work, neutron transport is modelled through the steady-state Boltzmann transport equation. Under this assumption, time dependence is neglected and the system is treated as stationary. Consequently, only the spatial, angular and energy dependence of the particle flux is considered.

For the making of this thesis version 5.1 was used [34]. The program is run on Cresco 6, ENEA's own High Performance Computing Cluster [35]. A simulation can employ up to 1200 CPUs simultaneously, generally taking from 10 minutes to 8 hours depending on the amount of surfaces, tallies and particle histories requested.

A generic MCNP input file consists of a text file where 5 sections can be usually identified:

- **Geometry**: The cells are constructed by taking the defined surfaces and either joining or intersecting them with each other. Then a material ID must be assigned to fill the cell with matter (ID is set to 0 if the cell is void).
- **Surfaces**: They are defined using the MCNP standard geometries and by specifying their location, size and occasionally shape. Examples of these surfaces are planes, spheres, cylinders, cones and parallelepipeds.
- **Materials**: A material is created by assigning it an ID and listing all of the elements that it's made of, either by using mass or atomic densities.
- **Source**: MCNP provides a generalized source capability that allows independent probability distributions to be assigned to energy, time, position and direction. It has built-in analytical functions like Watt, Maxwellian, Gaussian, isotropic, cosine and monodirectional distributions. Particular biases can also be applied through dedicated functions.
- **Settings**: Here the parameters of the simulations are set. They include numerical parameters, like the number of particle histories to simulate, and physical parameters, like which type of particles should the program simulate.
  Then the requested tallies are listed [36].

3.2.1. Tallies

Tallies are the tools used to estimate physical quantities of interest during a Monte Carlo simulation. A tally is a statistical estimator that accumulates contributions from particle histories as they undergo interactions and transport through the geometry. Typical quantities evaluated through tallies include neutron flux, reaction rates, energy deposition, dose and particle current.
Each tally is defined by its type, the region of space over which it is applied and optionally by energy, angle or time bins. All tally results are provided together with an associated statistical uncertainty, expressed as the relative error.

Surface current tallies The surface current tally (F1) evaluates the net number of neutrons or photons crossing a specified surface. For each particle history, MCNP records every crossing of the defined surface and assigns a positive or negative contribution depending on the direction of motion relative to the surface normal. The tally thus represents the particle current through the surface.

For this reason the F1 tally is sensitive to both the geometry of the surface and the angular distribution of the particle field.
If angular binning is applied the particles will be sorted according to the cosine of the angle between the particle's direction and the normal to the surface in question. This allows for the characterization of directional anisotropies in the radiation field.

Cell flux tallies Cell flux tallies (F4) are volume-averaged estimators that compute the neutron flux within a given cell. It's evaluated by accumulating the total path length travelled by all particles within the cell and normalizing it to the cell volume.
For a given cell of volume V, the flux estimated by an F4 tally can be expressed as

$$\phi = \frac{1}{V} \sum_i \ell_i \tag{3.1}$$

where ℓ_i is the path length travelled by the i-th particle inside the cell.
When energy binning is applied the summation is performed independently for each specified energy interval, resulting in an energy spectrum.
Due to their intrinsic averaging over the cell volume, F4 tallies do not provide information on local spatial gradients or angular anisotropies of the radiation field. For this reason, they are complemented by mesh tallies and point detector tallies, which allow for a more complete spatial characterization.

Point detector tallies The point detector tally (F5) evaluates the particle flux at a specific point in space. It does so by analytically computing the probability that particles emitted from the source or produced at collision locations reach the detector position without undergoing further interactions. This means that for each collision event, MCNP calculates the particle's contribution to the detector by accounting for divergence and scattering along the path between the event location and the detector.
Since the F5 tally does not rely on particles physically reaching the detector through random transport, it is most effective in regions of low particle density where direct other more direct tallies would suffer from poor statistics. In this sense the F5 tally is a form of variance reduction.
The result is independent of the size of surrounding cells or meshes, since the tally region, a set radius sphere, is superimposed over the geometry.

Mesh tallies Mesh tallies allow to overlay a regular Cartesian three dimensional grid over the geometry, where each mesh element (voxel) counts as the scoring volume over which the tallied quantity is averaged. Common tallied quantities are flux or deposited

energy.
Choosing the correct voxel size implies a trade off between spatial accuracy and statistical uncertainty: smaller mesh elements allow for finer spatial detail but they reduce the number of particle histories contributing to each voxel, increasing the relative error of the tally.
From a computational standpoint, mesh tallies employ the same estimators used for standard cell tallies, like track-length estimators for flux (fmesh4) [36].

Tally	Quantity measured	Region of scoring	Units
F1	Particle current	Surface	particles
F2	Scalar particle flux	Surface	particles/cm^{-2}
F4	Scalar particle flux	Cell	particles/cm^{-2}
F5	Scalar particle flux	Point	particles/cm^{-2}
F6	Energy deposition	Cell	MeV g^{-1}
F7	Fission energy deposition	Cell	MeV g^{-1}
F8	Pulse-height	Detector volume	counts per energy bin
FMESH4	Scalar particle flux	Mesh voxel	particles/cm^{-2}

Table 3.1: Overview of MCNP tallies. The units of measurement are all normalized per source particle.

3.3. Variance Reduction Techniques

Variance reduction techniques were employed to obtain statistically reliable results within reasonable computational time. The weight windows map, generated using ADVANTG in a previous work, were included to bring the relative error below 0.5%.
ADVANTG [37] is a Monte Carlo tool that computes an importance map based on an adjoint flux solution and automatically produces spatial and energy dependent weight windows. These weight windows guide particle transport by preferentially splitting particles in high importance regions, thus increasing the amount of particles simulated in that area, and rouletting those in low importance regions.
This leads to an improvement in efficiency without biasing the physical solution, since less particles are used to sample regions of no interest or where the accuracy is already good enough [37][38][39].

3.4. Nuclear Data

The study utilises cross sections taken from the Fusion Evaluated Nuclear Data Libraries (FENDL 3.1c). They contain neutron, proton and deuteron induced reactions up to a typical energy of 150 MeV [40]. It assembles the most suitable nuclear data for fusion applications selected from available nuclear data libraries, like ENDF/B-VIII.0, and JEFF-3.2 [41].

4 | GENeuSIS

4.1. GENeuSIS' Goals

The General Experimental Neutron System Irradiation Station (GENeuSIS) is a modular and customizable neutron irradiation test bed developed to reproduce radiation environments representative of those faced by components and diagnostics in ITER. While Monte Carlo simulations can accurately predict neutron and photon fields in ITER, experimental validation of radiation effects on electronics requires test environments that closely mimic the spectral characteristics of the radiation field in specific locations of the reactor. GENeuSIS addresses this by altering the neutron field produced by a 14 MeV D–T source through a carefully selected combination of shielding and moderating materials.
In particular, GENeuSIS has been conceived to replicate the neutron energy spectra relevant to selected regions of the ITER Equatorial Ports [42]. Two main configurations of the test bed have been designed for two distinct reference radiation environments in the ITER Equatorial Port 12:

- GENeuSIS-I: optimized to reproduce the harder neutron spectrum found close to the vacuum vessel, immediately behind the closure plate (ISS region).
- GENeuSIS-II: targets the more attenuated neutron spectrum characteristic of the Port Cell, where a significant fraction of ITER electronics will be installed (PCSS region).

The present work focuses on GENeuSIS-II, as it is specifically intended for irradiation tests on electronic components such as SRAM memories. From this point forward, any mention of GENeuSIS will refer to the second iteration (GENeuSIS-II).

4.2. GENeuSIS' Structure

GENeuSIS is composed of a stack of planar layers made of different materials placed in front of the neutron source (i.e., FNG), enclosing an inner irradiation cavity where the devices under test are located.

The materials, thickness, and order of the plates were optimized through Monte Carlo simulations to tailor the neutron energy spectrum and flux intensity.
Overall GENeuSIS is 80 cm long, 60 cm wide and 55 cm tall.
The composition is visible in figure 4.1 and 4.2, with the exception of two 200 µm thick cadmium sheets placed just before and after the cavity. The cadmium layer at the end of the cavity presents an opening with the same dimensions as the cavity to leave its backside open for access.
In the original tests the assembly was placed in a concrete bunker, visible in figure 4.3, in order to take into account the backscattering effect of the walls. Moreover the assembly is sitting on a large aluminum plate to support it. In this thesis the model was extended by adding the supports that connect the aluminum plate to the floor, as described in the "Additions to the model" section. The origin of the coordinate system, that will be later employed to define the locations of tallies and activation foils, is the tritiated target visible on the left of the GENeuSIS assembly in figure 4.1. Consequently, the source coordinates coincide with the origin.
The cavity is offset with respect to the Z axis, as the cavity floor sits at Z=-8 cm and it's top side at Z=22 cm.

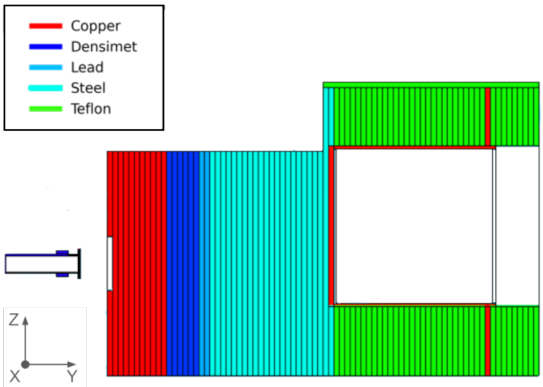

Figure 4.1: Tritiated target (left) and assembly, cut at the X=0 plane and viewed from the side.

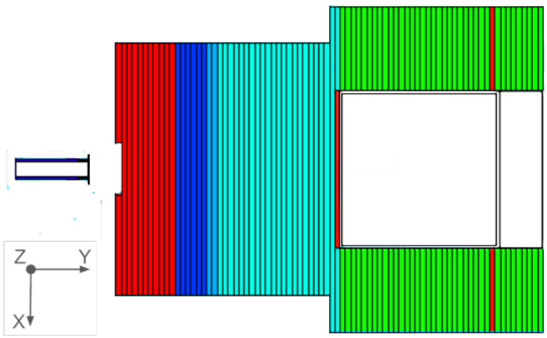

Figure 4.2: Tritiated target (left) and assembly, cut at the Z=0 plane and viewed from the top.

Figure 4.3: Bunker walls.

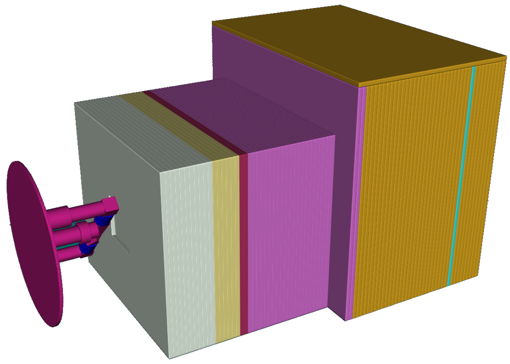

Figure 4.4: 3D view of GENeuSIS in front of the FNG target neutron source.

A key feature of GENeuSIS is the relatively large irradiation cavity, with dimensions of approximately 30x30x30 cm. This volume is designed to accommodate electronic boards, detectors and activation foils while ensuring sufficient neutron fluence for statistically meaningful measurements. At the same time, the size of the cavity introduces potential spatial and angular variations to the inner radiation field, making its detailed characterization a critical aspect of the test bed validation. Assessing neutron and photon field homogeneity, as well as identifying possible anisotropies, is therefore essential to define optimal locations and orientations for the devices under test.

4.3. Target Spectrum

The neutron energy spectrum in the ITER Equatorial Port Cell is significantly attenuated and moderated with respect to the primary 14.1 MeV fusion neutron source. As shown in Fig. 4.5, the spectrum is dominated by neutrons in the epithermal and fast energy range below a few MeV followed by a non-negligible thermal component. Under nominal D-T ITER operation (Inductive 500 MW fusion power scenario, neutron yield $1.77{\times}10^{20}$ n/s), the neutron flux in the Port Cell is of the order of 5×10^5 n/cm^2/s, leading to integrated fluences up to 5×10^{11} n/cm^2 over representative operational periods relevant for the qualification of electronic components [42][43].
GENeuSIS has been designed to reproduce this spectral distribution, enabling accelerated irradiation campaigns: owing to the high neutron yield of the Frascati Neutron Generator, Port Cell equivalent fluences can be achieved within irradiation times ranging from a few hours to a few days, since the flux inside the GENeuSIS cavity can reach values as high

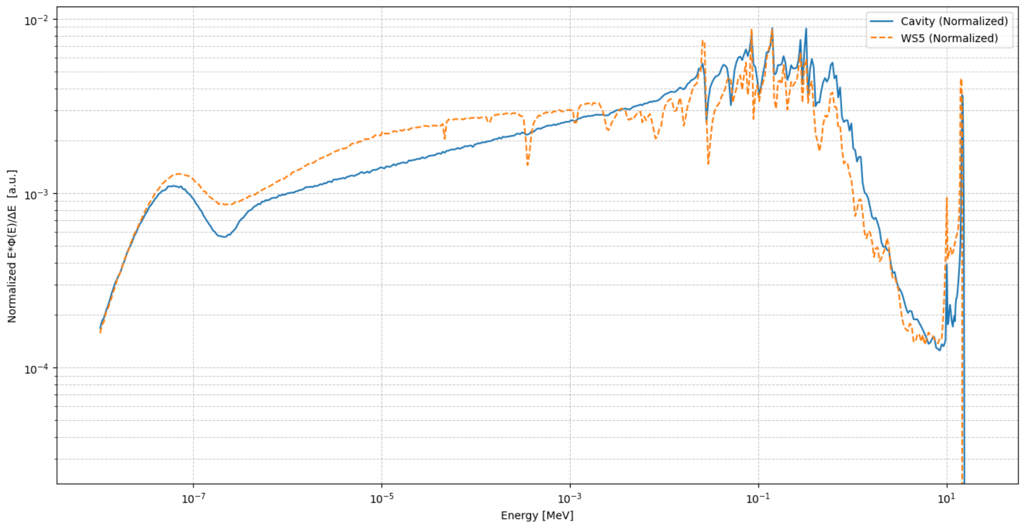

Figure 4.5: The original spectra simulated for the workstation 5 and the average spectrum inside of the cavity compared with each other.

as 8.6×10^5 n/cm^{2}s when FNG's yield is around 2×10^{10} n/s. This makes GENeuSIS a suitable platform for the study of radiation effects on electronics under ITER relevant Port Cell conditions.

4.4. Criteria to evaluate the neutron spectra

In the original analysis, the cavity-averaged neutron energy spectrum was divided into 175 energy groups [44]. For each group, the ratio of the GENeuSIS spectrum to the ITER reference spectrum was calculated, and the configuration was then optimized to minimize the average of these ratios. This yielded a final absolute average difference of 35.8%.
Other metrics that can be used as criteria to evaluate the similarities of the spectra are:

- **The Pearson correlation** (r): it measures the linear correlation between the two spectra indicating how similar their shapes are regardless of magnitude.
- **The root mean square relative difference** (R_{rel}): it quantifies the average bin-by-bin relative deviation between the spectra, giving a measure of local differences across the energy range.
- **The root mean square ratio** (R_{mag}): it evaluates the overall magnitude difference between the spectra by comparing the sum of the squared values of each bin, highlighting global scaling effects.

The equations used to calculate them can be found in Appendix A.

The calculation for the original spectrum was repeated using the same tally but by employing a 709 energy bins spectrum instead. The plots are visible in figure 4.5 and by applying the metrics described above the results are: $r = 0.888$, $R_{mag} = 1.02$, $R_{rel} = 0.349$ and the mean absolute difference is 28.2%. Therefore, it's possible to see how the R_{mag} and R_{rel} functions behave: R_{mag} is close to 1 since the two spectra have been normalized, while R_{rel} is in line with the mean absolute difference obtained through more conventional means. If the spectra were not normalized the Pearson correlation would be the same, but the other values would change to $R_{mag} = 1.25$, indicative that the ITER spectrum is around 25% higher in magnitude, and $R_{rel} = 1.5$.

4.5. Additions to the model

In order to increase the accuracy of the simulations with respect to the experiments that will be carried out the FNG facility, The GENesuSIS supporting structure has been added to the MCNP model. It's made entirely of aluminum and it's composed by multiple I beams and slabs, some with screws and guide rails to allow for adjustment along both the z and y directions (where the Y axis points away from FNG and the Z axis points toward the roof) as shown in figure 4.7.
It also has a HDPE removable "U" shaped band going around the backside (visible in orange in figure 4.7).

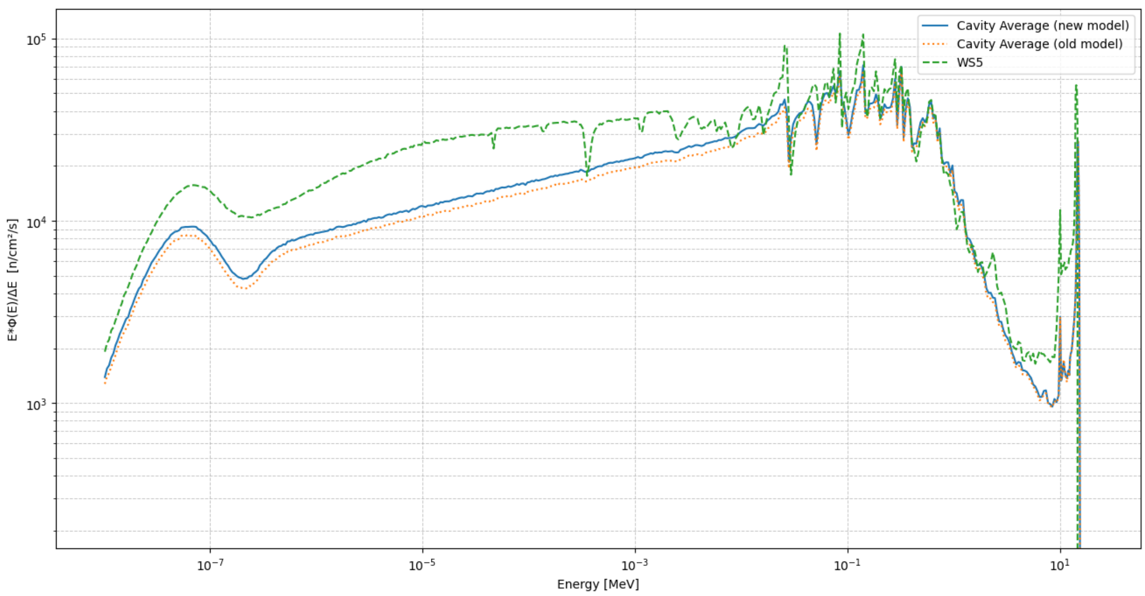

Figure 4.6: The old spectrum compared to the one obtained with the addition of the aluminum base. In this figure the were not normalized to show the different magnitudes.

This addition slightly altered the spectra, mostly by populating the thermal region, as visible in figure 4.6. The overall flux increased by around 12% throughout the whole cavity.
This had the effect of actually increasing the accuracy with respect to the ITER reference spectra, as, for the unnormalized case, the Pearson correlation r value improved from 0.888 to 0.895, the R_{rel} from 1.5 to 1.37 and R_{mag} from 1.25 to 1.12.
The whole set of the following results have been calculated using the improved model.

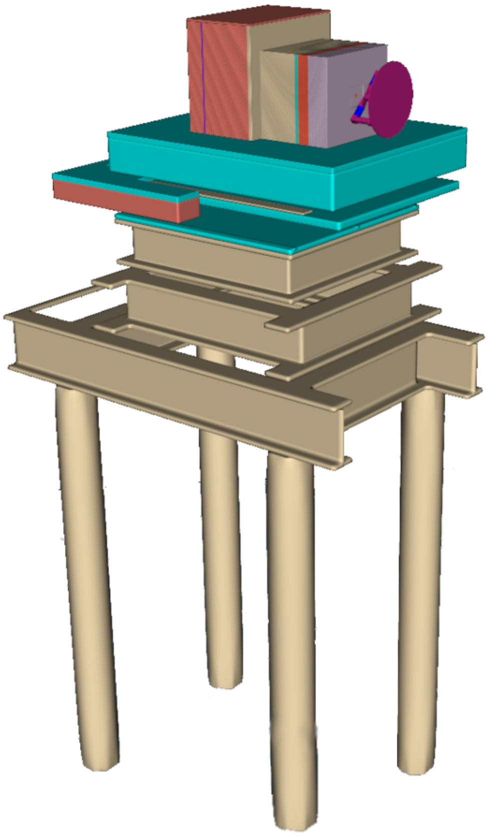

Figure 4.7: Starting from the top: GENeuSIS and FNG's tritiated target, the aluminum plate (in azure) and the underlaying structure that sits on the floor.

5 | Nuclear analysis for the GENeuSIS project

5.1. Neutron field analysis

The spectra presented in the previous section have been obtained by tweaking GENeuSIS' composition and structure until the average neutron spectra in the cavity matched ITER's. This has been done by applying an f4 tally over the volume of the cavity. As a consequence, there is uncertainty in how the spectra can vary from point to point, from both the aspect of flux intensity and energy distribution. The goal of this chapter is to provide a comprehensive analysis of these anisotropies, making future tests on the assembly bed more informed and thus more precise. Since MCNP tallies are normalized per source particle, the results are expressed per source neutron. To obtain absolute values, the tallies were multiplied by 2×10^{10} n/s, corresponding to the neutron yield of the FNG source.

The results presented in this section refer exclusively to the neutron field present in the irradiation cavity.

5.1.1. Mesh tallies

The first test performed on the cavity was a mesh tally, covering the whole 30x30x30 cm space with a voxel size of a 1x1x1 cm. Voxel sizes smaller than that have been tested and they require an excessive amount of computing time, without providing any additional information.

The results are then plotted using ParaView software [45] with a logarithmic scale.

The highest neutron flux in the cavity is observed at the lower edge closest to the FNG source, rather than directly in front of it. This behaviour is due to the assembly centre being positioned 6.5 cm above the coordinate origin (i.e., the FNG source location). As a result, there is more material above the source available to reflect neutrons downward than below it to reflect them upward, leading to an asymmetric flux distribution.

The results highlight that there is half an order of magnitude difference in flux between the highest flux voxel and the lowest.
This indicates that the neutron field inside the cavity is not isotropic: such an aspect has to be taken into account while conducting specific experimental campaigns dedicated to specific purposes (e.g. cumulated dose effects on electronic devices).
These considerations neglect the energy distribution of the spectrum since the mesh in Figure 5.2 and 5.3 only tally neutron flux. In MCNP additional insights can be gained by applying a tally card that imposes an energy binning to the mesh, thus generating a mesh for each considered energy bin.
A four bin energy structure has been selected, in order to get a more detailed insight on the neutron energy distribution inside the cavity and, at the same time, provide results with a reliable statistics (the bin edges are 10^{-11}, 10^{-6}, 10^{-3}, 1, 20 MeV). The most interesting one is the first bin, showed in figure 5.4, while the other three showed a distribution that matched closely the total one. This energy range is associated to thermal neutrons (thermal energy is around 10^{-8} MeV).

Figure 5.1: F4mesh spectrum of the cavity mid-plane (X=0), logarithmic. The contour lines values are indicated in the legend of the plot ($7{\times}10^5$, $6{\times}10^5$, $5{\times}10^5$, $4{\times}10^5$, $3{\times}10^5$).

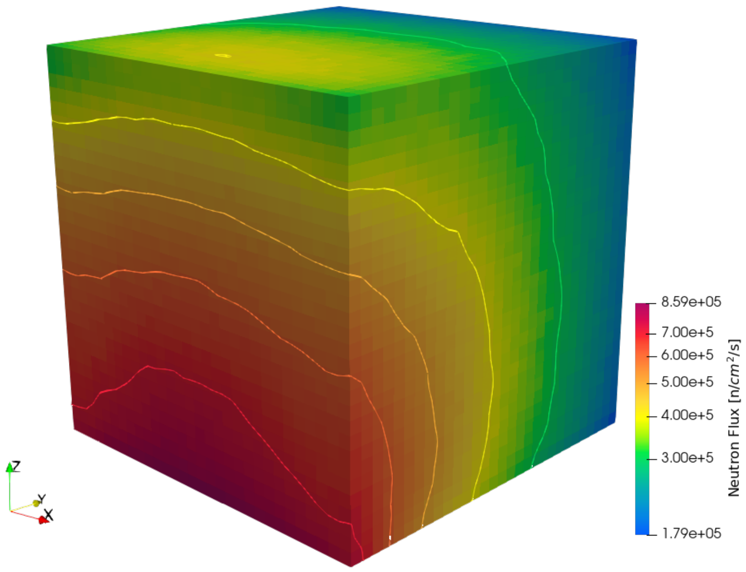

Figure 5.2: F4mesh spectrum of the cavity, logarithmic. The contour lines values are indicated in the legend of the plot ($7 \times 10^5,\ 6 \times 10^5,\ 5 \times 10^5,\ 4 \times 10^5,\ 3 \times 10^5$).

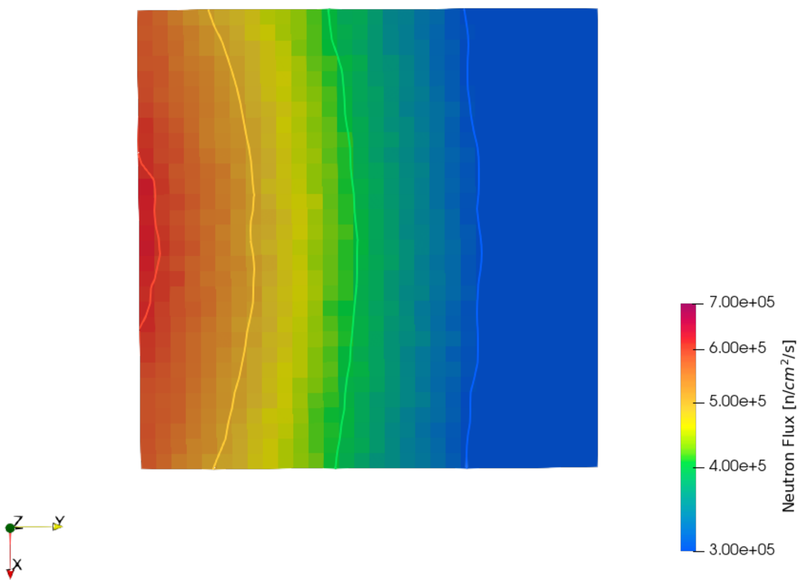

Figure 5.3: Section along the mid-plane of the neutron flux map (Z=8) viewed from the top, logarithmic. The contour lines values are indicated in the legend of the plot ($7 \times 10^5,\ 6 \times 10^5,\ 5 \times 10^5,\ 4 \times 10^5$).

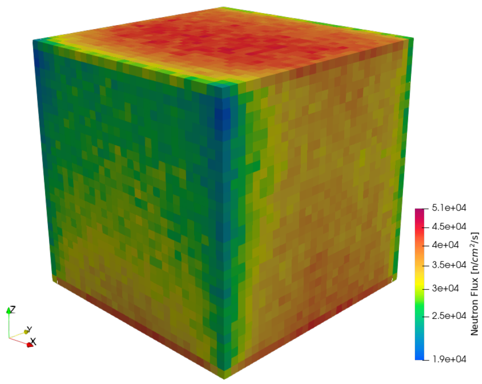

Figure 5.4: Thermal neutrons distribution inside the cavity, logarithmic.

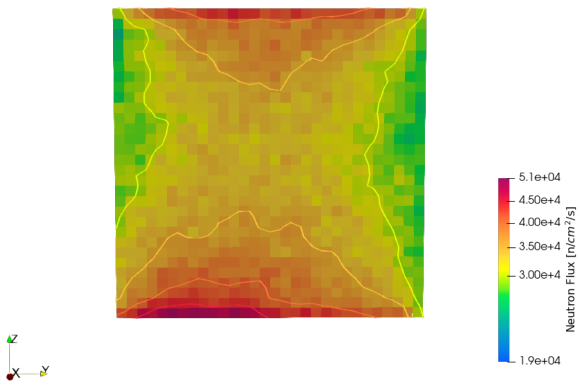

Figure 5.5: Section along the mid-plane of the thermal neutron flux map 5.4, logarithmic. The contour lines values are indicated in the legend of the plot (4.5×10^5, 4×10^5, 3.5×10^5, 3×10^5).

5.1.2. F5 tallies

Since the detectors, activation foils, and test memories that will be placed in the cavity can be small compared to the cavity itself (a typical NAND chip has a die size of 6x8 mm), it's useful to probe the neutron field with an array of f5 tallies to to characterize the neutron field throughout the cavity.
Initially this array was composed by 48 f5 tallies, each with a radius of 1 cm, distributed throughout the whole cavity. After the first simulations it was confirmed that the results, as expected, were perfectly symmetric with respect to the x=0 plane and for this reason one half of the array was removed to save on compute time.
These tallies have been set up with the standard 709 groups energy binning [46] and will output spectra that range from 5×10^{-9} to 20 MeV. These can then be compared to the ITER Port Cell reference spectrum to check how isotropic the cavity is with respect to deviations from said spectrum.
Figure 5.7 and figure 5.8 display how the tallies were positioned in the cavity, the tally number and the flux value measured by each tally. The tallies are located on two parallel planes, one in X=0 and one in X=13. Figure 5.7 the tallies of the X=0 plane (and the three bottom ones of the X=13 plane), while 5.8 shows how the tallies flux values relate to the one obtained for tally 15, which is located in X,Y,Z=(0, 0, -6.5), close to the point of highest flux. A similar array with X=7 instead of X=13 was tested and it provided almost identical spectral characteristics, it can be found in Appendix A.

Figure 5.8 displays the flux of each f5 tally with respect to tally 15. It is easier to see here than from the mesh tallies that the flux is not constant throughout the cavity and that placing a component or a detector closer to the source will have a great effect.
Now, the variations within the energy spectrum must be investigated.

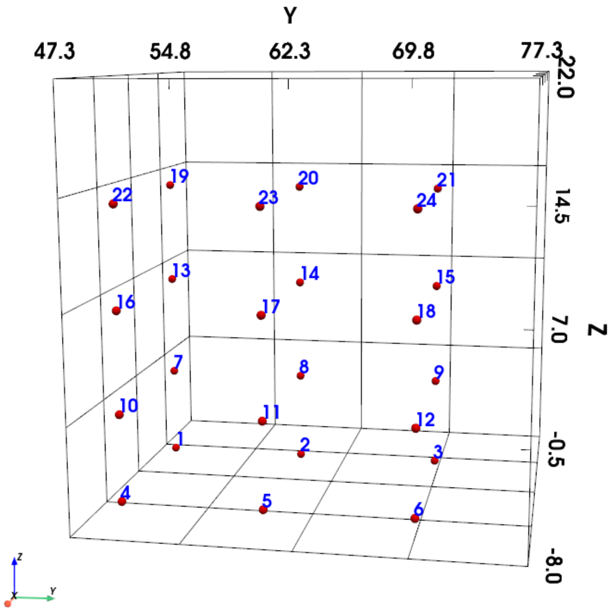

Figure 5.6: All of the f5 tallies in the cavity.

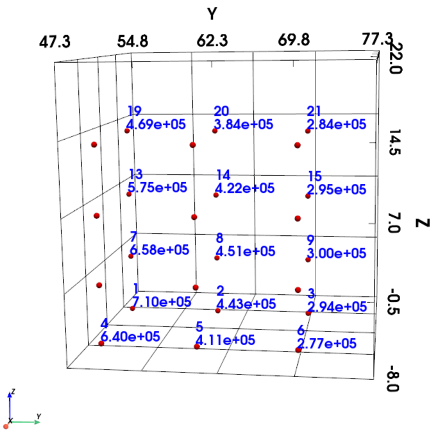

Figure 5.7: F5 tallies along the X=0 plane, plus three from the X=13 plane. The values are in $n/(\mathrm{cm}^2\,\mathrm{s})$.

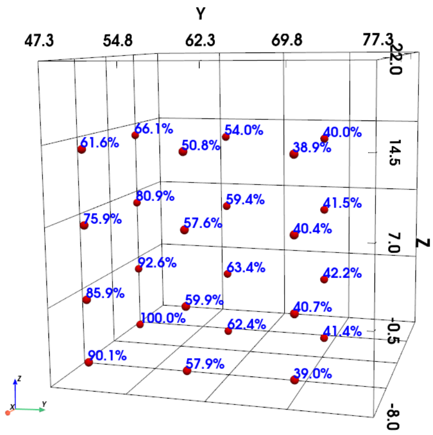

Figure 5.8: Tallies' flux values with respect to the tally 1.

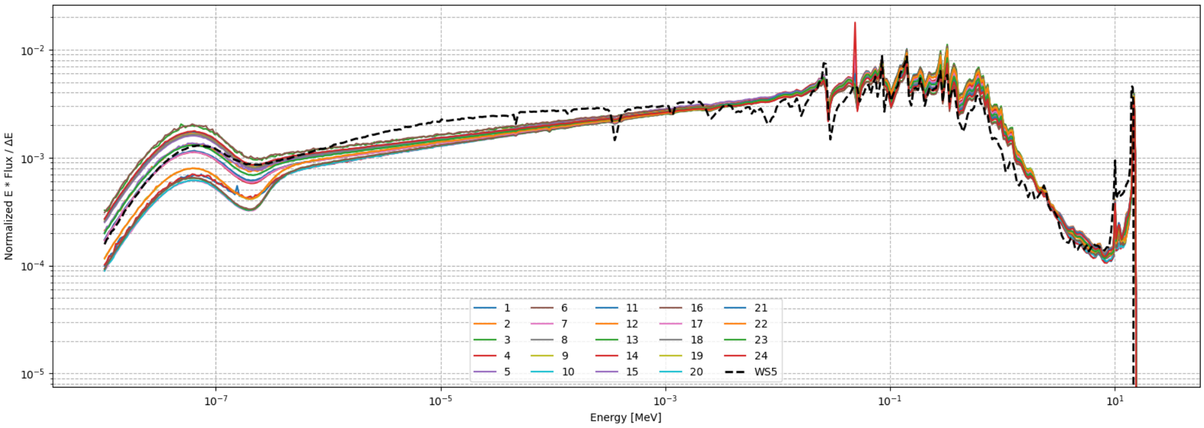

Figure 5.9: Spectra inside the cavity, calculated by means of F5 tallies.

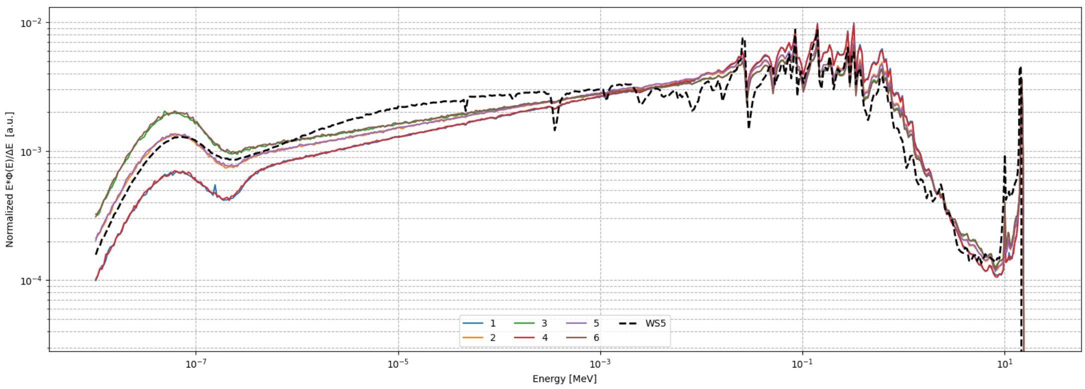

Figure 5.10: Spectra 1 to 6, belonging to Z=-6 plane, calculated by means of F5 tallies.

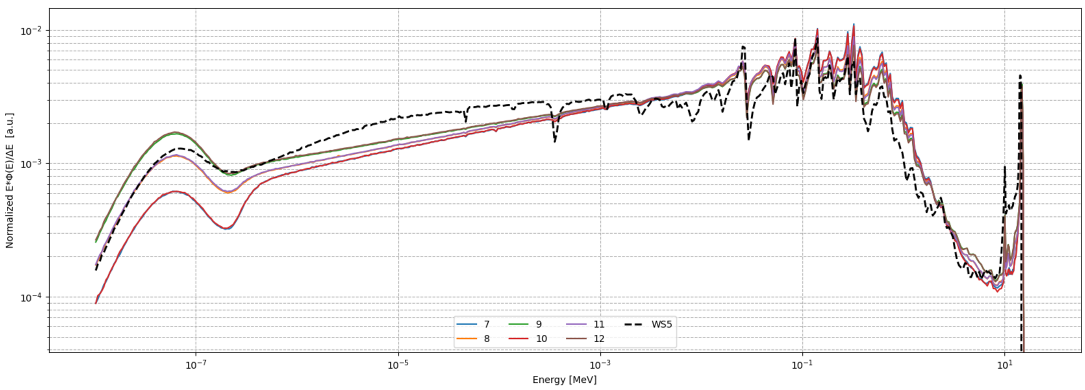

Figure 5.11: Spectra 7 to 12, belonging to Z=0 plane, calculated by means of F5 tallies.

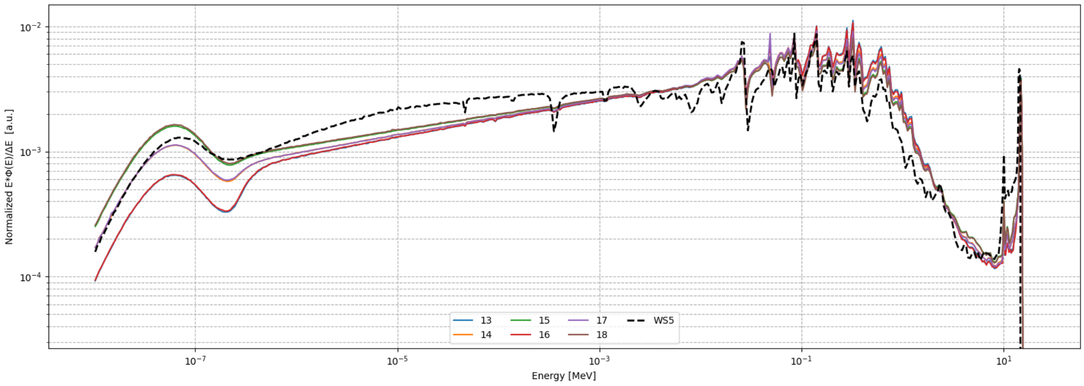

Figure 5.12: Spectra 13 to 18, belonging to Z=7 plane, calculated by means of F5 tallies.

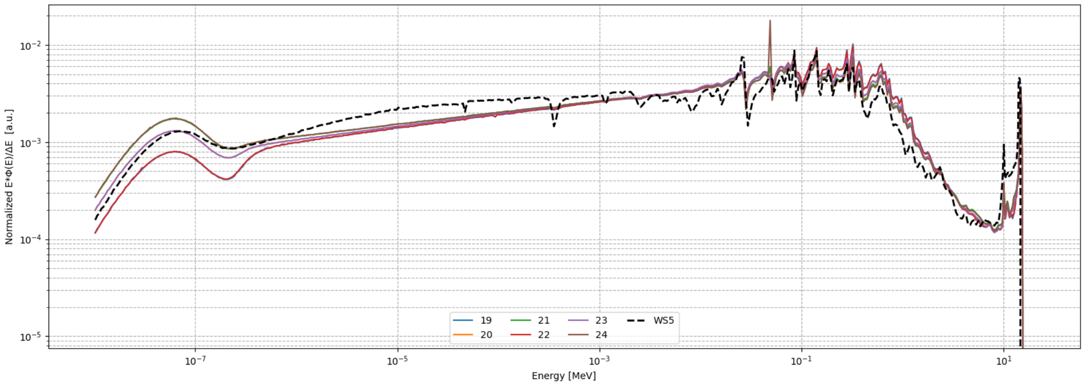

Figure 5.13: Spectra 19 to 24, belonging to Z=14 plane, calculated by means of F5 tallies.

To better compare spectra calculated at different positions inside the cavity, each spectrum was normalized by dividing every energy bin by its total flux, accounting for the non uniform flux distribution within the cavity.
Figure 5.9 shows the neutron energy spectra of all the f5 tallies described above. The plots highlight that the spectra are quite similar, with the largest deviations from each other occurring in the thermal region.
From figures 5.10, 5.11, 5.12 and 5.13 it can be seen that there is very little dependence on the X axis, as the spectra that lie on the same X coordinate are almost indistinguishable from one another. This is consistent with the spectra calculated for X=7 present in Appendix A.
Table 5.9 presents the statistical analysis of the spectra calculated with the F5 tally, aimed at identifying the spectrum that best approximates the ITER reference. The study indicates that tally 2 provides the most reliable representation of the ITER spectrum, as it exhibits one of the highest Pearson correlation coefficients (r) and the best relative error (R_{rel}). Its spectrum is plotted below in figure 5.14. It is located at X,Y,Z=(0, 60.0,

-6.0), which places it near the bottom of the cavity, at the origin along the X-axis and close to the centre of the cavity along the Y-axis.

Tally	(x, y, z)	Pearson r	R_{rel}	Mean Abs % Diff
1	(0.0, 50.3, -6.0)	0.88239	0.42836	36.853
2	(0.0, 60.0, -6.0)	0.90146	0.30013	23.504
3	(0.0, 70.0, -6.0)	0.90298	0.34626	26.672
4	(13.0, 50.3, -6.0)	0.88002	0.43863	38.387
5	(13.0, 60.0, -6.0)	0.88700	0.30371	23.899
6	(13.0, 70.0, -6.0)	0.89057	0.38388	28.455
7	(0.0, 50.3, 0.0)	0.87294	0.46076	39.112
8	(0.0, 60.0, 0.0)	0.89087	0.35198	28.209
9	(0.0, 70.0, 0.0)	0.89969	0.32909	26.372
10	(13.0, 50.3, 0.0)	0.87773	0.45715	39.832
11	(13.0, 60.0, 0.0)	0.89044	0.32865	26.350
12	(13.0, 70.0, 0.0)	0.89702	0.33473	26.493
13	(0.0, 50.3, 7.0)	0.87145	0.45573	38.440
14	(0.0, 60.0, 7.0)	0.88780	0.36055	28.925
15	(0.0, 70.0, 7.0)	0.89632	0.33216	26.883
16	(13.0, 50.3, 7.0)	0.87837	0.44460	38.568
17	(13.0, 60.0, 7.0)	0.88731	0.33282	26.694
18	(13.0, 70.0, 7.0)	0.89693	0.33017	26.239
19	(0.0, 50.3, 14.0)	0.88153	0.40461	33.661
20	(0.0, 60.0, 14.0)	0.89356	0.30972	24.624
21	(0.0, 70.0, 14.0)	0.89961	0.33075	26.348
22	(13.0, 50.3, 14.0)	0.88548	0.39779	33.980
23	(13.0, 60.0, 14.0)	0.89356	0.30972	24.624
24	(13.0, 70.0, 14.0)	0.89497	0.36314	27.000

Table 5.1: Comparison of normalized spectra against the WS5 reference spectrum.

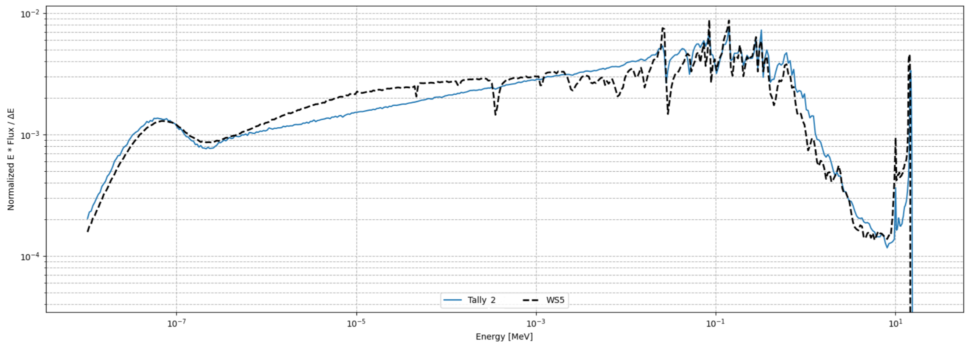

Figure 5.14: The spectrum of tally 2 compared to the reference ws5 tally.

Since the biggest variations in the spectra can be seen in the thermal region it's worth investigating it further. By setting a maximum energy for a neutron to be considered "thermal" it's possible to estimate how much of the total flux is comprised of thermal neutrons.

The results (figure 5.15) show that the flux in this energy window can vary significantly and that it's the most responsible for the differences with the ITER reference spectrum, since the tallies with the lowest thermal fraction are also the lowest performing one from table 5.1.

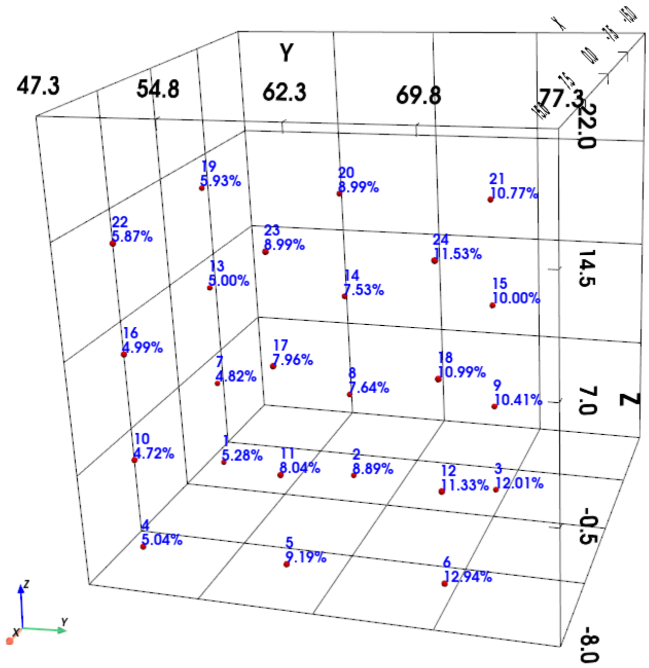

Figure 5.15: How much of each f5 tally spectrum is comprised by neutrons with energy lower than 10^{-6}MeV.

Yet overall the results show that across the cavity the spectral shape varies negligibly with respect to the cavity average spectrum that was used as a metric to model the cavity itself.
Another way to confirm this is to select the two spectra that differ the most and compare them without normalization. The results show a Pearson r of 0.985 and an R_{mag} of 2.6. These values are consistent with previous results and demonstrate that the overall spectral shape remains almost unchanged, while the flux magnitude varies significantly.
In conclusion the cavity average tally can be considered a reliable tool in assessing the cavity's spectral properties, although it neglects big variations in overall neutron flux and some minor ones in the thermal energy range. The latter has also been proven as the source of the biggest differences with the ITER reference spectrum.

5.1.3. Angular tallies

For the GENeuSIS project, it is important to investigate whether the neutrons exhibit one or more preferential streaming directions. As explained earlier, electronic components often have highly asymmetrical nanostructures, and their orientation relative to a neutron source affects the extent of radiation-induced effects.
One way to test for this form of anisotropies is to use f1 tallies with an angular binning card, where the upper and lower bounds of the bins are provided as either cosines or degrees. The tally works by by defining a series of concentric cones around the surface's normal vector, a unique vector that is perpendicular to the surface and that's placed at its centre. The angle formed by the cones' inner and outer walls is determined by the cosines in the input.
It follows that these tallies are independent of the azimuthal direction and incident particle's location.
30 bins are defined in terms of the cosine, spanning the interval from -1 to +1 and corresponding to scattering angles from 180° to 0°. The bin spacing is more refined in the forward and backward directions, where the angle is close to 0°, and coarser around 90°, providing an increased angular resolution in the regions where more scattering is expected.

The cavity inner volume was divided into two equal parallelepipeds in order to increase the number of surfaces to tally, as shown in figure 5.16. These boxes, referred to as "RPP 1" and "RPP 2" ("RPP" as rectangular parallelepiped), have six faces, each associated with an outward-pointing normal vector defined with respect to the center of the box. For this reason, some of the tally plots in figure 5.19 have been mirrored. This ensures that the front and back, as well as the bottom and top, are consistently oriented in the same direction. Figures 5.17 and 5.18 provide a visualization of the different orientations

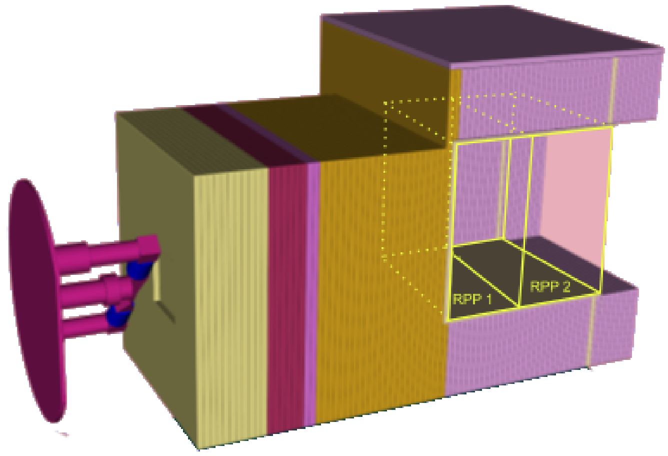

Figure 5.16: GENeuSIS cut from one side to show the different surfaces used to tally the angular distributions.

described above.
To better highlight differences between bins, the radial scale was chosen as a compromise between linear and logarithmic representations. A purely logarithmic scale diminishes the apparent differences across the roughly two orders of magnitude in flux, while a linear scale does not fully capture the overall variation.
The numerical results are plotted in figure 5.19. All of the plots are normalized for bin width.
The cavity's preferential streaming direction is the Y-axis, since, as visible in figure 5.19, around the 0° mark "RPP 1 front" has the highest flux values of any plot, alongside "RPP 1 back" and "RPP 2 back".
The difference, when compared to the walls (X and Z direction), is around 5 to 6 times for "RPP 1" and almost an order of magnitude for "RPP 2". This implies that further back in the cavity the flux is more streamlined and less uniform.
The plots also show a significant amount of backscattering along the Y direction, caused by reflections from the cavity's inner walls, as visible from the angles at which the particles return. This results in an angular distribution of neutrons that is influenced by the assembly's missing closure plate on the backside. Such behaviour is consistent with expectations and highlights how the assembly geometry can affect the spatial distribution of radiation within the cavity, which should be considered when interpreting experimental measurements.
Figure 5.17 shows that the flux maintains the cone shape observed in tally 81 throughout

the cavity, as evidenced by the wider particle exits in tallies 151 and 161 compared to 91 and 101. Similar observations can be made from Figure 5.18. Another notable point is that, for RPP 1, the bottom section emits nearly twice as many particles into the cavity as the top section. In contrast, for RPP 2, the difference between top and bottom emissions is only about 10%.

In both RPP 1 and RPP 2, the bottom surface sees more particles entering the cavity than it sees leaving it, and the opposite is true for the top surface. This is another form of asymmetry, although limited in magnitude, that can be attributed to both the off center nature of the cavity and the larger amount of material below GENeuSIS (the support structure) compared to above it.

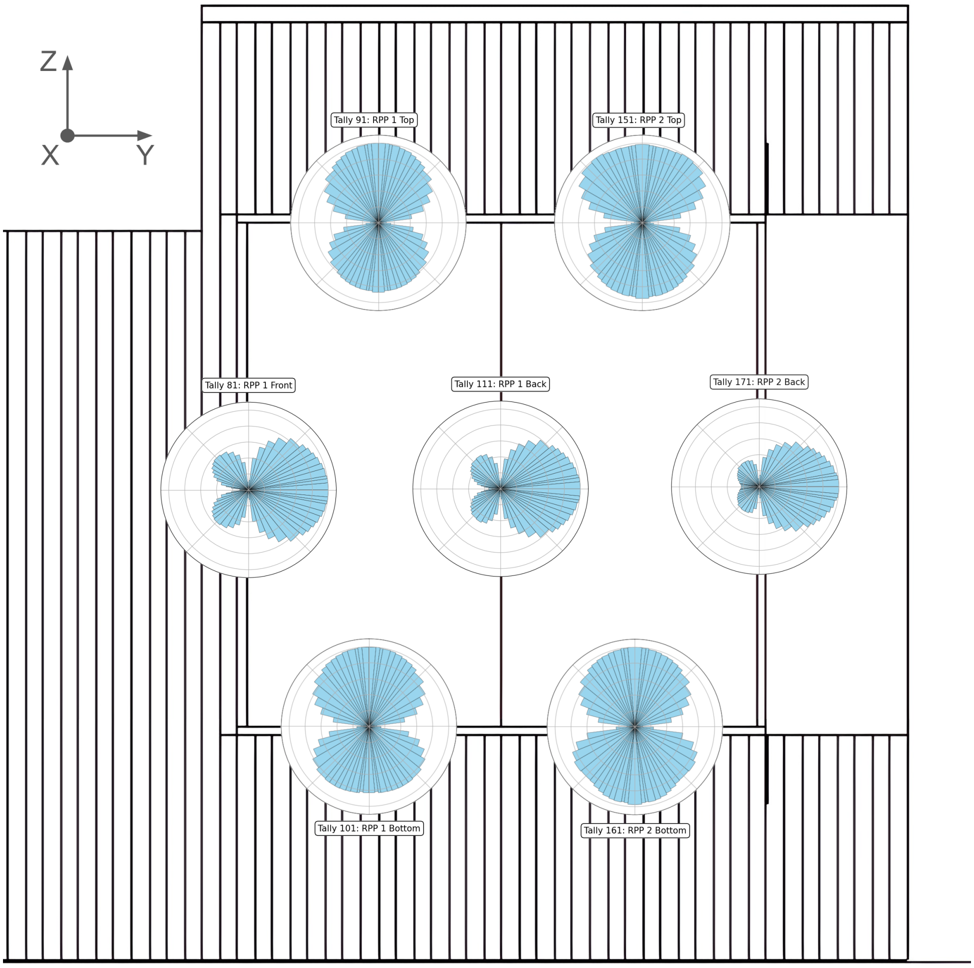

Figure 5.17: Side section of GENeuSIS assembly showing the angular distribution of neutrons inside the inner cavity. The FNG source is placed on the left.

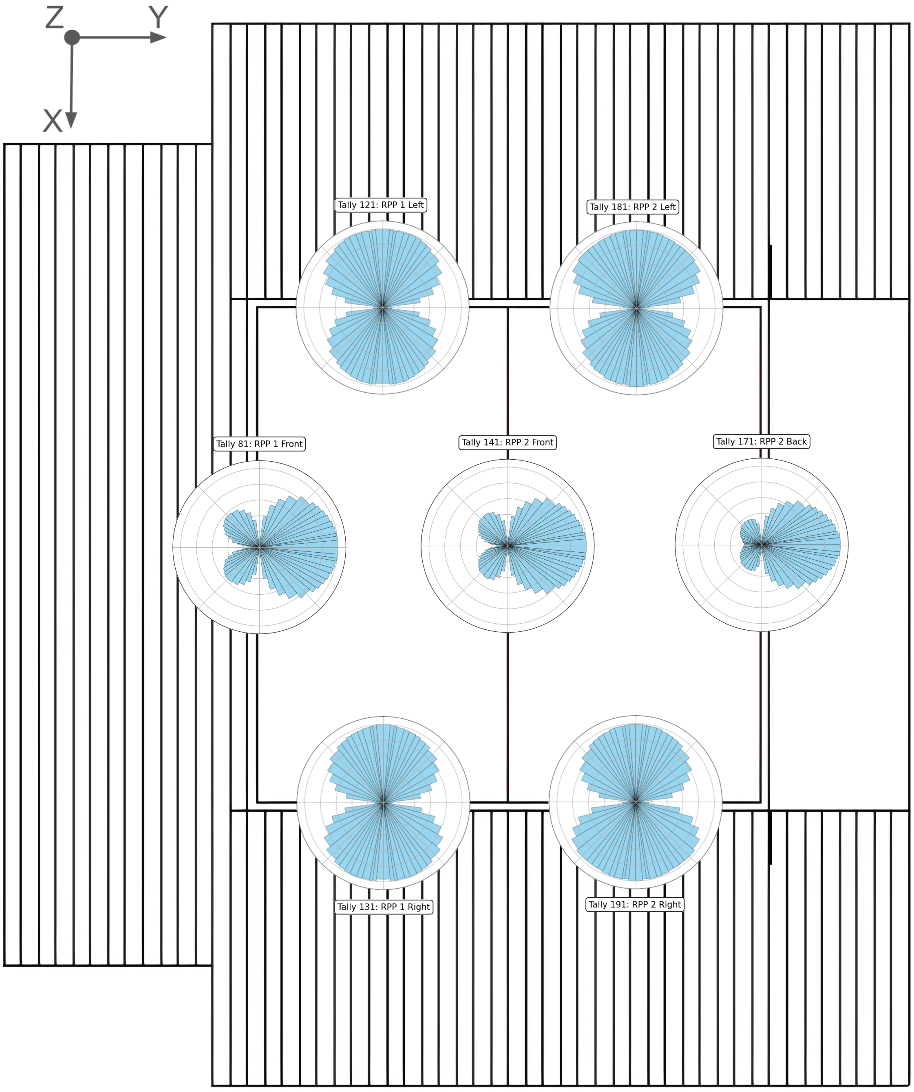

Figure 5.18: Top section of GENeuSIS assembly showing the angular distribution of neutrons inside the inner cavity. The FNG source is placed on the left.

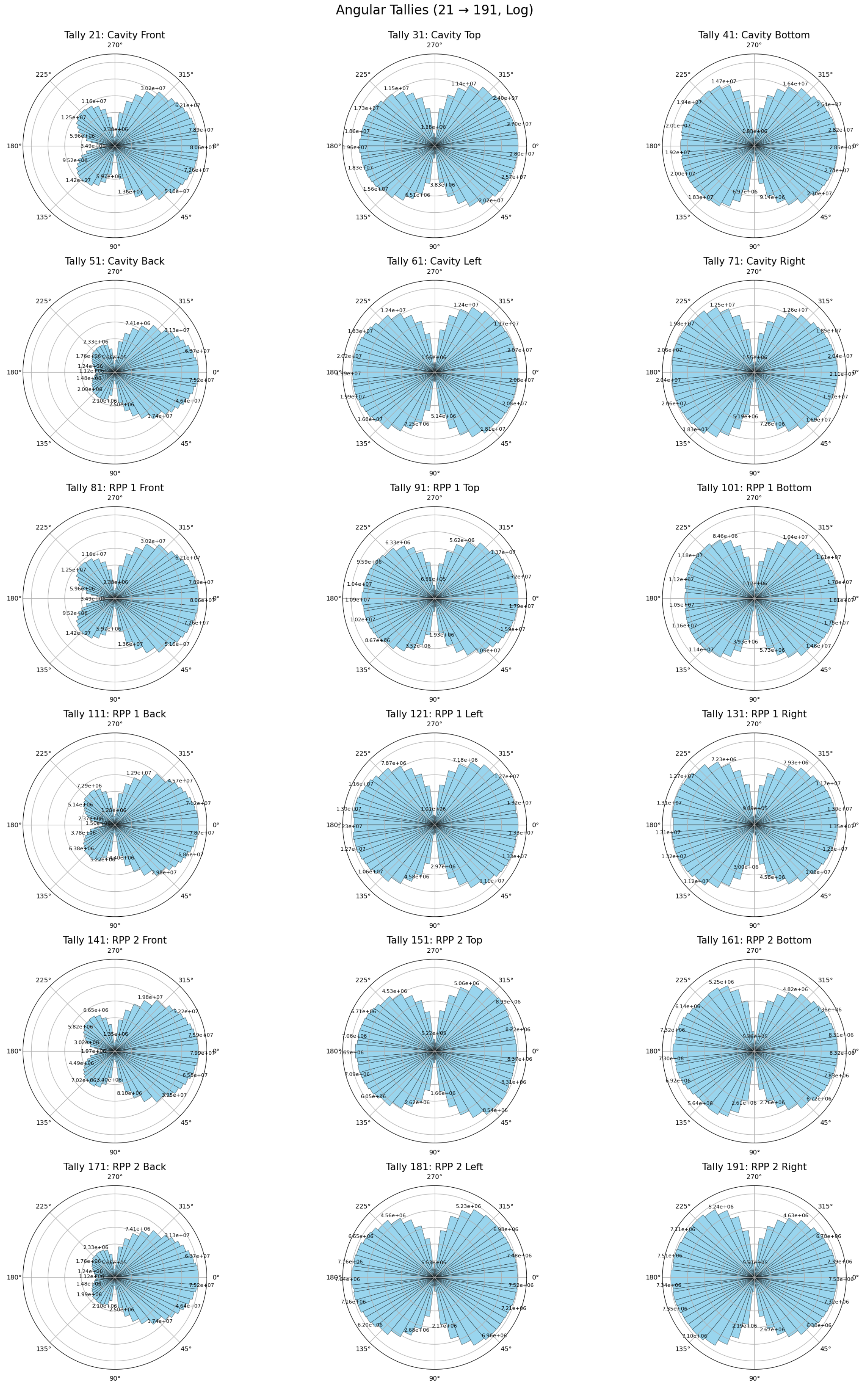

Figure 5.19: Angular distribution of the neutrons for all the tallies positions.

5.2. Tests with DIAMON

The Direction-aware Isotropic and Active neutron MONitor (DIAMON) is a portable neutron detector that can deliver good spectrometric capability and a quasi-isotropic response, from thermal to high energies (up to 20 MeV for the low energy version). It consists of a polyhedral moderator body made of high-density polyethylene (HDPE) which hosts a matrix of semiconductor-based thermal neutron sensors [47].
It has been used to characterize neutron fields from experimental campaigns performed at the CERN-EU high-energy Reference Field (CERF) and at the Bern medical cyclotron, showing good agreement with the Monte Carlo simulations and the established neutron monitoring instruments like the Berthold LB 6411 [48].
Its isotropic response and extensive validation make the DIAMON an excellent candidate to characterize the neutron field inside GENeuSIS. However, since its physical dimensions are not negligible with respect to those of the cavity and its body is mostly made of HDPE, the presence of the detector itself may perturb the neutron field. To address this concern, the detector was modeled in MCNP by assuming that it is comparable to a HDPE truncated dodecahedron enclosed in a 2 mm aluminium shell.
Successively two tallies were defined: an F4 tally in the cavity space excluding the volume occupied by the DIAMON, and an F5 tally with a 1 cm radius at the center of the HDPE. Two separate simulations were performed: one with the DIAMON in the cavity and one without.

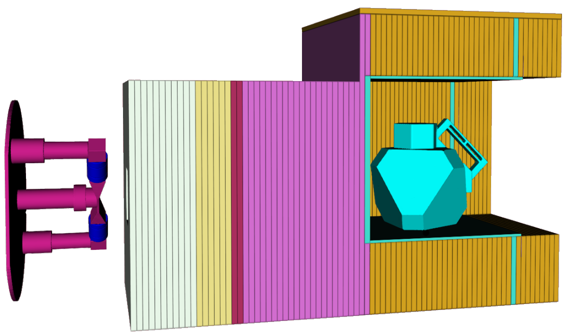

Figure 5.20: Section of the GENeuSIS MCNP model showing the DIAMON detector inside it.

The results are shown in 5.21. The most notable effect of the HDPE occurs at the core of the DIAMON detector, where high-energy neutrons are moderated, populating the thermal and epithermal regions. This behavior is expected and does not affect the measurements, as the detector can reconstruct the unperturbed spectrum using its response functions.

Tally 54 similarly shows an increase in the thermal population throughout the cavity, as neutrons are moderated in the center and scatter off the inner walls. This effect is likely to be detected by the DIAMON. Determining the exact magnitude of this perturbation would require further study, but it can be considered negligible for the purposes of this thesis.

Tally	Pearson r	R_{rel}	R_{mag}
15	0.769	0.39	1.038
54	0.995	0.11	1.037

Table 5.2: Comparison of Spectral Metrics between runs with the DIAMON and without it (the latter is used as the reference spectrum)

Table 5.2 shows that, in the space around the DIAMON within the cavity, the average deviation from the reference spectrum is approximately 10% for each bin (R_{rel}), while the average magnitude (R_{mag}) increases by about 4%.

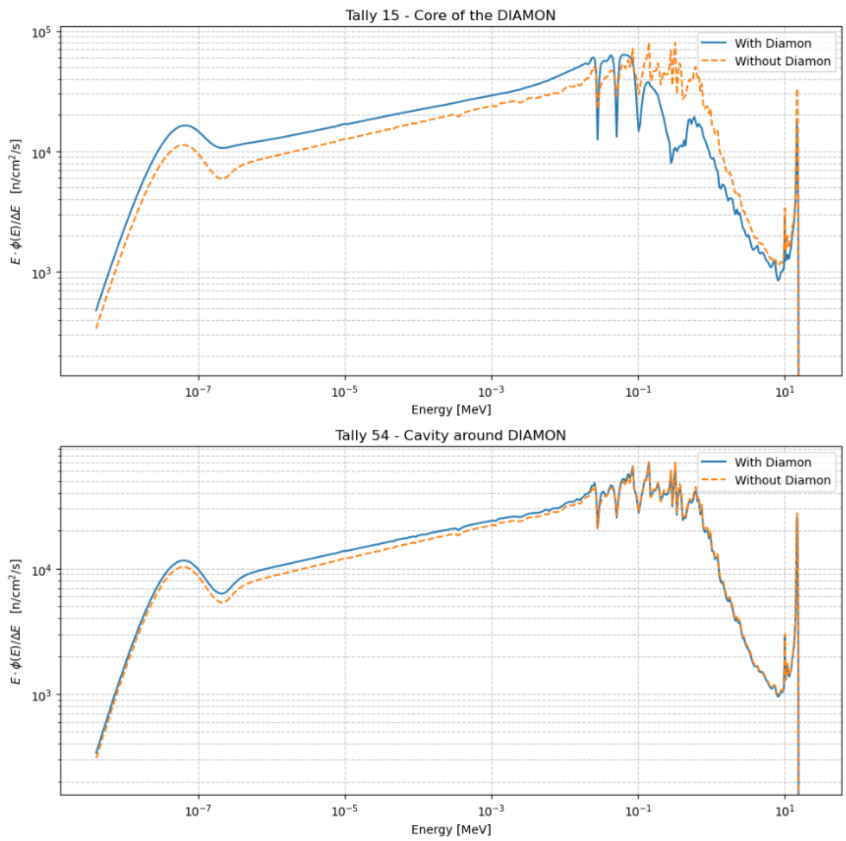

Figure 5.21: Comparison between the spectrum of the entire cavity (Tally 54) and that of the cavity containing the DIAMON detector (Tally 15).

5.3. Activation foils

Activation foils are a well-established and widely used technique for characterizing neutron fields, primarily because they effectively minimize contributions from gamma radiation, which can otherwise interfere with neutron measurements. The method relies on exposing carefully selected materials to a neutron flux, after which the induced radioactivity is measured. This radioactivity arises from neutron–nucleus interactions within the foil material, producing isotopes whose activity can be precisely quantified. By choosing nuclear reactions with well-known, energy-dependent cross sections, activation foils provide an integrated response to the neutron spectrum over a defined energy range. This makes them particularly valuable for obtaining a spectrum-averaged characterization of the neutron field, offering insights that are difficult to achieve with direct detection methods alone.
Activation foils are compact and do not require data or power cables, allowing them to be placed in tight spaces without perturbing the neutron spectra. Their main drawback is that, being passive detectors, they do not provide real-time measurements; instead, they must be quickly transferred to a spectrometer (HPGe - High Purity Germanium detector installed at the FNG laboratory) to measure the emitted decay gamma radiation.
Simulating activation foils in MCNP beforehand is important because it allows the feasibility of the measurement to be assessed. The foil must accumulate sufficient activity during the allotted experiment time so that, even after being removed from the assembly and transferred to the HPGe detector, it retains enough activity to enable an accurate measurement. The selection of the activation foils, including both material composition and geometrical dimensions, was based on a review of FNG's own foil repository.
The selection of the activation foils, including both material composition and geometrical dimensions, was made by looking through FNG's own repository of foils.
After modelling the foils in MCNP, the reaction rates were calculated using F4 tallies combined with dosimetric cross sections.

5.3.1. Activation foils placement inside the GEneuSIS assembly

To sample the field across all of the regions of interest, four sets of activation foils locations were devised.

- One set was placed upstream of the cavity along the y axis (Z=0, X=0), between the moderating plates and aligned with the FNG source.
- Three additional sets were positioned along three different planes (fixed z) inside the cavity volume. The foils were only placed on the negative X side in two rows,

one in X=0 (positions 1, 4 and 6) and the other at X=-14 (positions 2, 3 and 5).

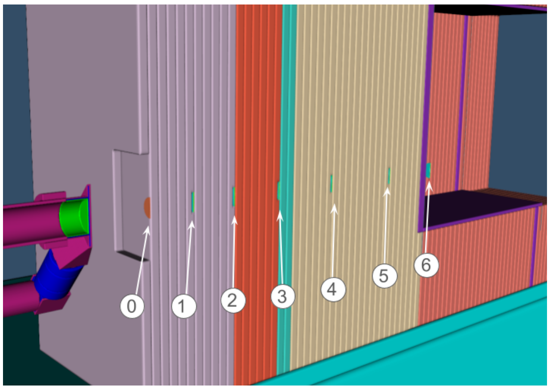

Figure 5.22: Before the cavity.

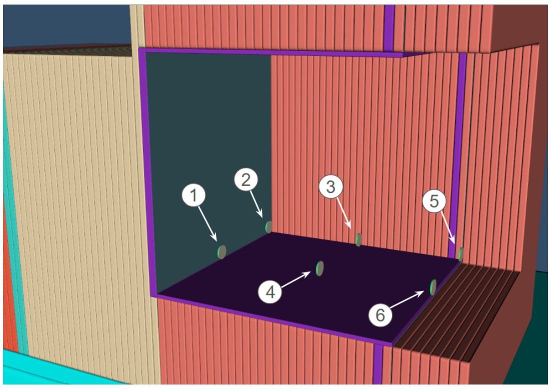

Figure 5.23: Z = -6.5.

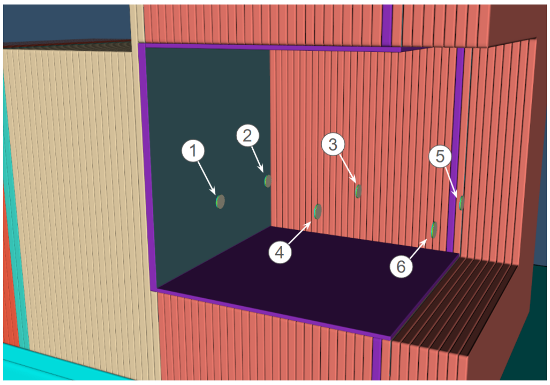

Figure 5.24: Z = 0.

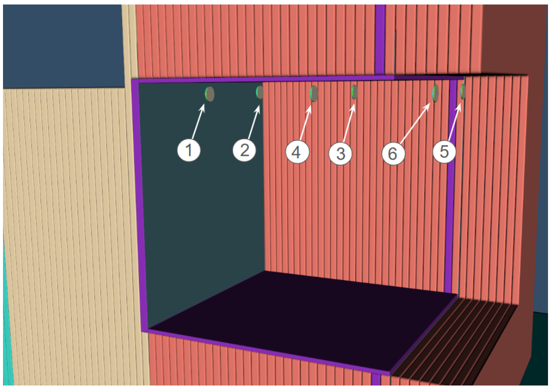

Figure 5.25: Z = 20

For each location, two distinct foil stacks were simulated. The first consisted of two foils with a radius of 1 cm, made of niobium and indium, both with a thickness of 1 mm. The second stack consisted of three foils, also with a radius of 1 cm, made of aluminium and nickel (1 mm thick) and gold (150 µm thick).
An additional single niobium foil (1 mm thick, 1 cm radius) was placed in front of the assembly, upstream of the cavity entrance, but only for the first set of locations. It's indicated by the label "0" in figure 5.22.

Number of foils	2
Foil materials	Nb, In
Foil radius	1 cm
Foil thickness	1 mm (each)

Table 5.3: Two-foil stack

Number of foils	3
Foil materials	Al, Ni, Au
Foil radius	1 cm
Foil thickness	Al, Ni: 1 mm
	Au: 150 μm

Table 5.4: Three-foil stack

The selected activation foils provide sensitivity across all of the neutron energy range expected inside the GENeuSIS test cavity, as visible from table 5.5.
The ^{197}Au$(n,\gamma)^{198}$Au reaction is particularly interesting because ^{197}Au is monoisotopic and exhibits a large thermal neutron capture cross section that extends all the way to epithermal energy ranges. This comes from the fact that, being a radiative capture reaction, it does not possess an energy threshold for neutron absorption, making it particularly suitable for activation analysis. Meanwhile reactions such as ^{58}Ni$(n,p)^{58}$Co, ^{27}Al$(n,\alpha)^{24}$Na and ^{93}Nb$(n,2n)^{92m}$Nb have well defined threshold energies, being mostly sensitive to fast neutrons [49].

Mat.	Reaction	Half-life	E_γ (keV)	$E_{\mathbf{thr}}$ (MeV)
Au	^{197}Au$(n,\gamma)^{198}$Au	2.696 d	412	–
In	^{115}In$(n,n')^{115m}$In	4.49 h	336	0.1
Ni	^{58}Ni$(n,p)^{58}$Co	70.82 d	811	2.9
Al	^{27}Al$(n,\alpha)^{24}$Na	14.96 h	1369	8.5
Nb	^{93}Nb$(n,2n)^{92m}$Nb	10.15 d	934	10.8

Table 5.5: Activation reactions and corresponding nuclear data [50].

5.3.2. Results

The reaction rate (RR) calculated through MCNP is obtained by integrating the product of the neutron flux spectrum and the energy-dependent microscopic cross section over energy:

$$RR = \frac{1}{V}\int_V \int_0^\infty \int_{4\pi} \phi(\mathbf{r},E,\Omega)\sigma(E)\,d\Omega\,dE\,dV \tag{5.1}$$

where $\phi(\mathbf{r},E,\Omega)$ is the neutron flux spectrum in the cell, $\sigma(E)$ is the microscopic reaction cross section for the selected nuclide and reaction, and V is the cell volume. The cross sections are taken from the radiometric (dosimetry) libraries provided with the nuclear data files.
The result of the integral is the volume averaged reaction rate per source particle per atom, which can then be multiplied by FNG's neutron yield and amount of atoms per foil to obtain the reactions per second [36]. The plots of the cross sections for the listed reactions can be found in Appendix A.
Looking at the results from all the setups, the reaction rates for the gold foils remain almost perfectly consistent regardless of position. This is because the cross section of Au-197 follows a 1/v trend, and in the positions analysed in GENeuSIS, a decrease in

total flux is almost always associated with an increase in the thermal and epithermal components.
For the first setup, where the foils have been placed in between the plates, it's evident that the foils most dependent on fast neutrons (Al, Ni, Nb, In) get progressively less and less activated as the amount of moderating material increases. Other effects, such as shielding of the foils placed before are to be excluded since simulations were only one foil stack was placed in the same position showed results that were almost identical, being off by 1% at most.
It's interesting to see how the Nb foils capture the uncollided fast neutrons. This effect is particularly evident by looking at figure 5.29 and 5.31: the central positions (1, 4 and 6) at Z=0, which are directly in line with the source, consistently have higher reaction rates compared to the Z=-6.5 counterparts, even though the latter are subject to a higher flux. This is due to the fact that the point of maximum flux, being off center with respect to the source, results primarily from numerous internal scattering events. A part of the fast neutrons, on the other hand, remains unscattered, and thus they predominantly contribute along the shortest path to the cavity (the path along the z=0 plane).
Another interesting result is how the ^{197}Au RR drops only in half when the foil is placed from the region of maximum flux to the region of lowest flux, even though the flux drops four fold.
This is actually consistent with the results from figure 5.15, which shows that the thermal neutrons flux of the lower total flux region is two times the one of the higher total flux region.
The same figure also displays how the first F5 tallies of the Z=0 plane have higher portions of the uncollided fast neutrons described above.
These results prove that the foils activation analysis, while less intuitive at first, can provide useful results in the scope of the spectral characterization of the cavity.

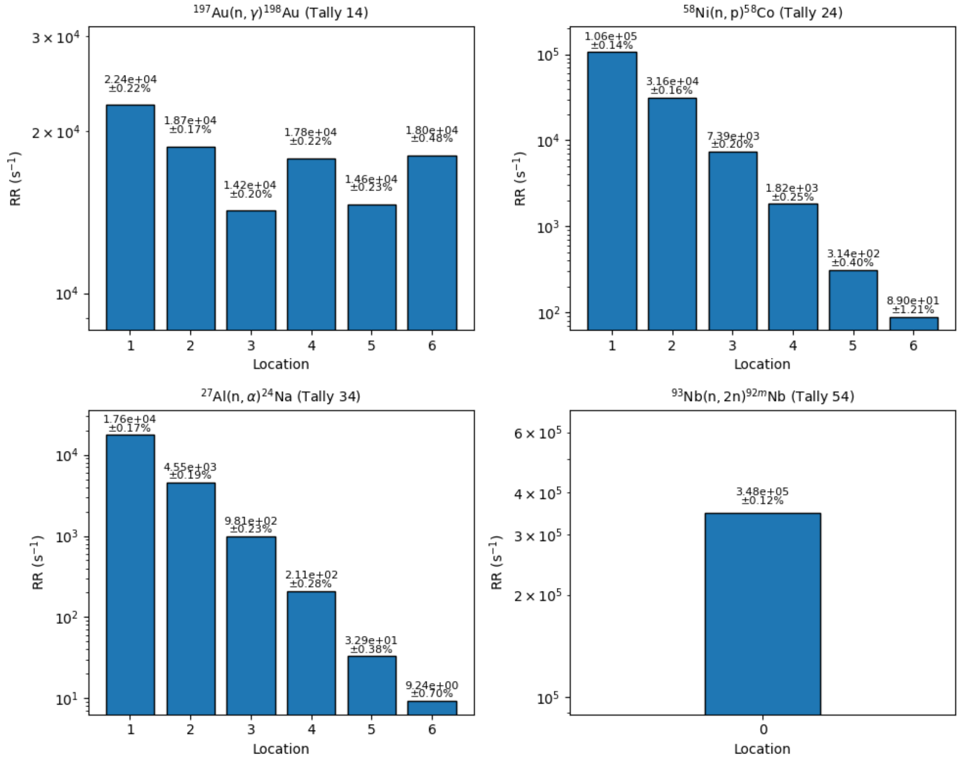

Figure 5.26: Upstream moderator region, three-foil stack (Al, Ni, Au, Nb)

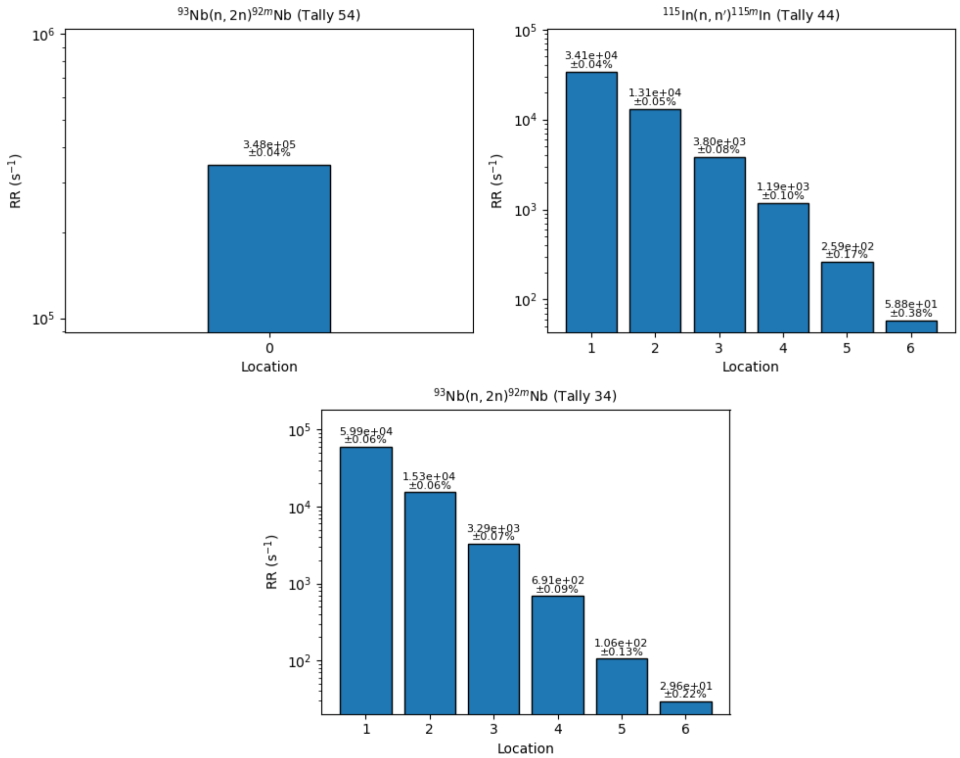

Figure 5.27: Upstream moderator region, two-foil stack (Nb, In)

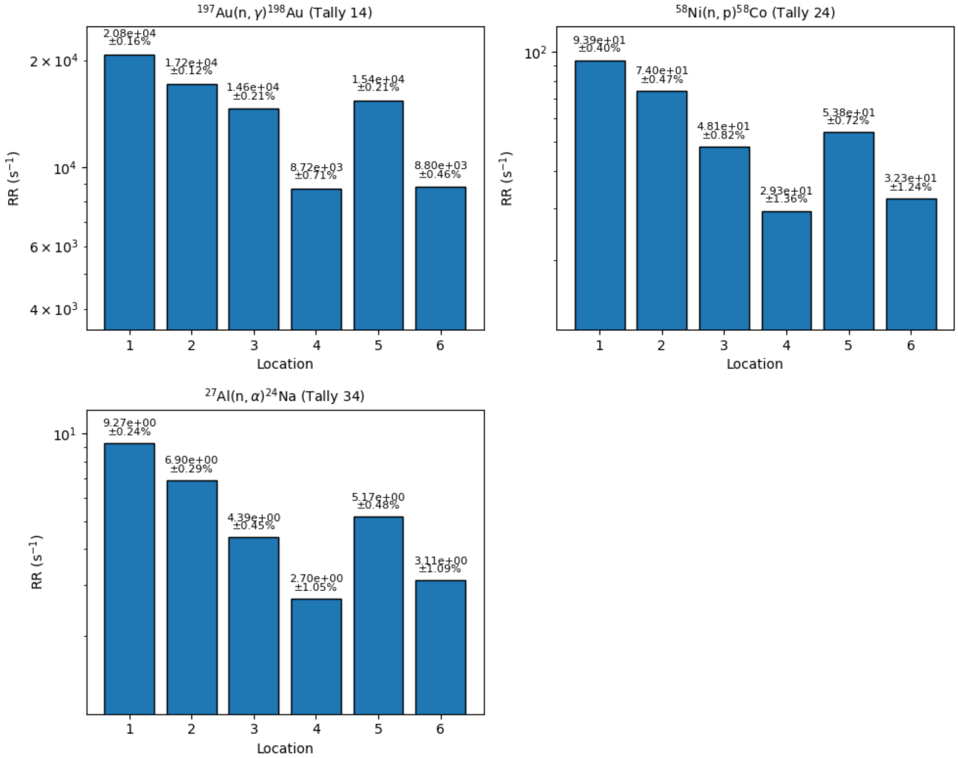

Figure 5.28: Cavity plane $Z = -6.5$, three-foil stack (Al, Ni, Au)

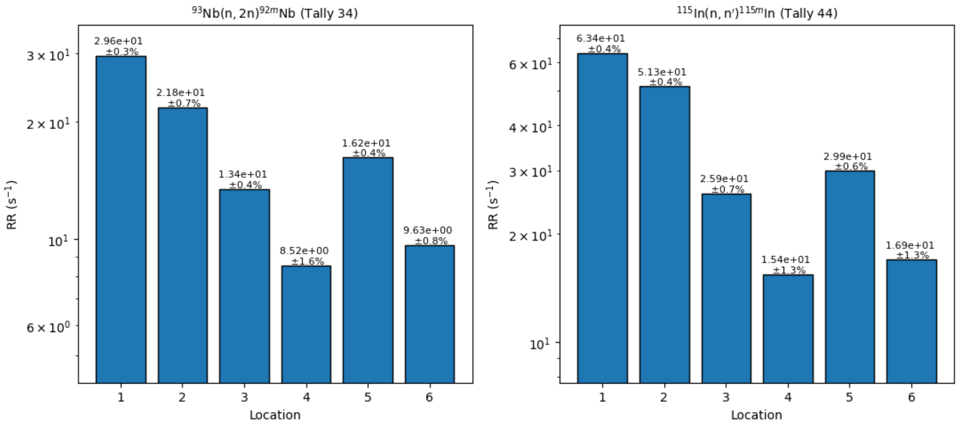

Figure 5.29: Cavity plane $Z = -6.5$, two-foil stack (Nb, In)

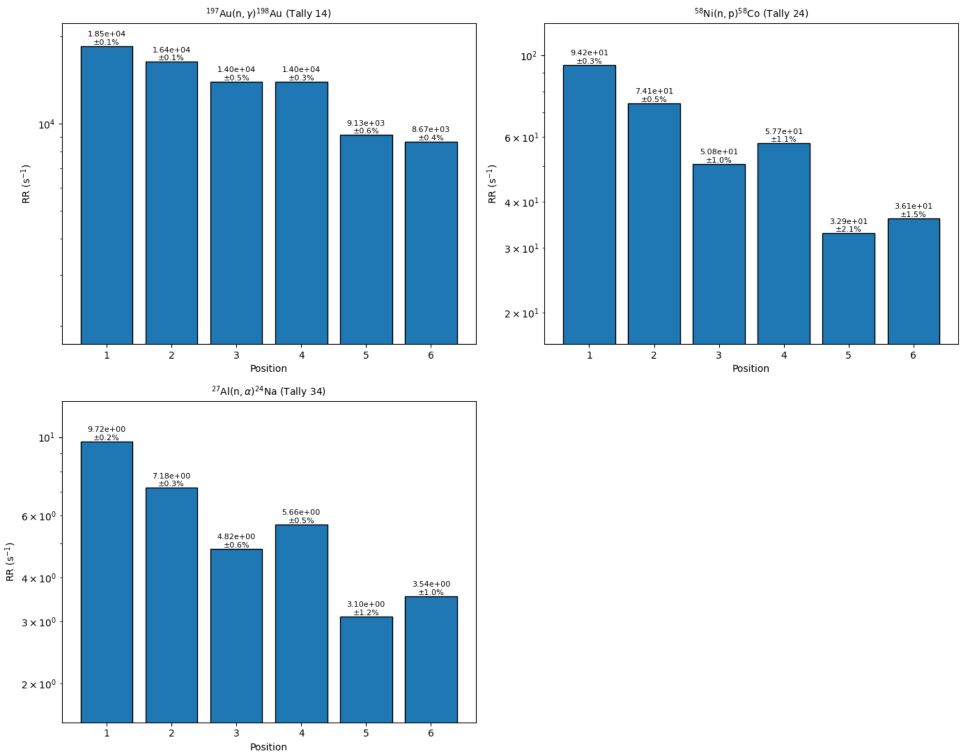

Figure 5.30: Cavity plane $Z = 0$, three-foil stack (Al, Ni, Au)

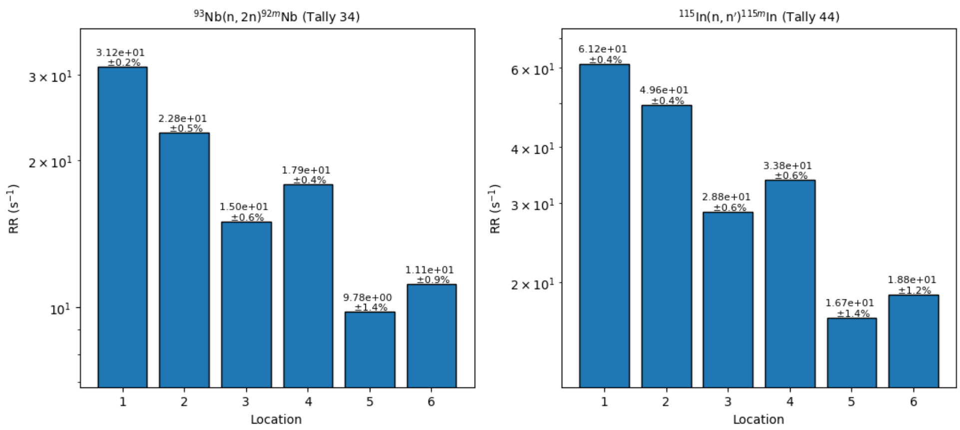

Figure 5.31: Cavity plane $Z = 0$, two-foil stack (Nb, In)

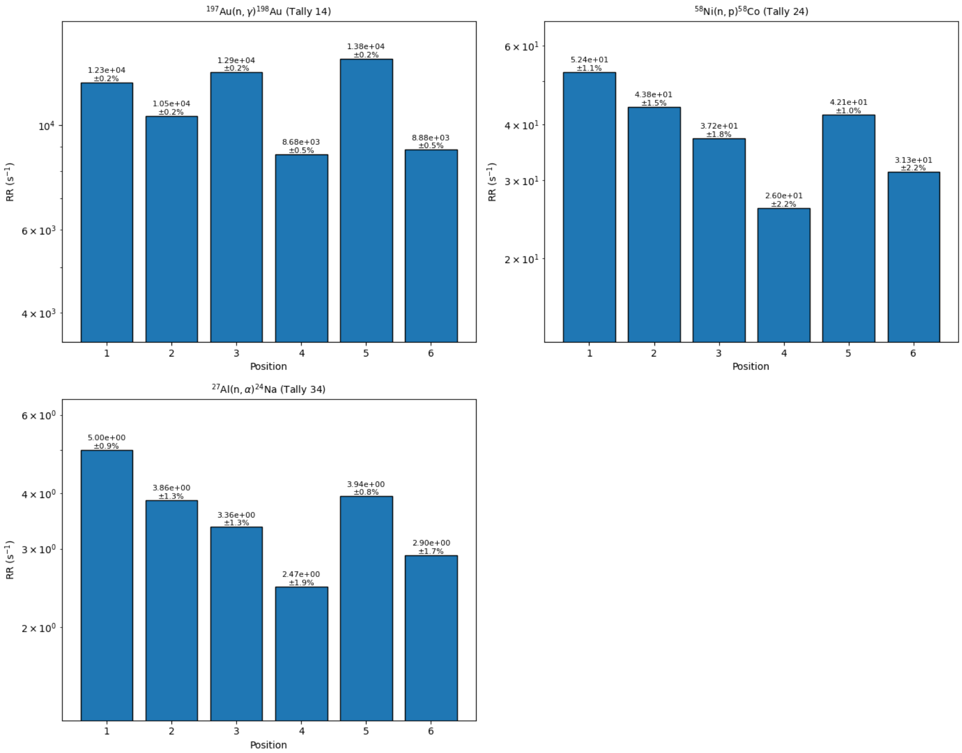

Figure 5.32: Cavity plane $Z = 20$, three-foil stack (Al, Ni, Au)

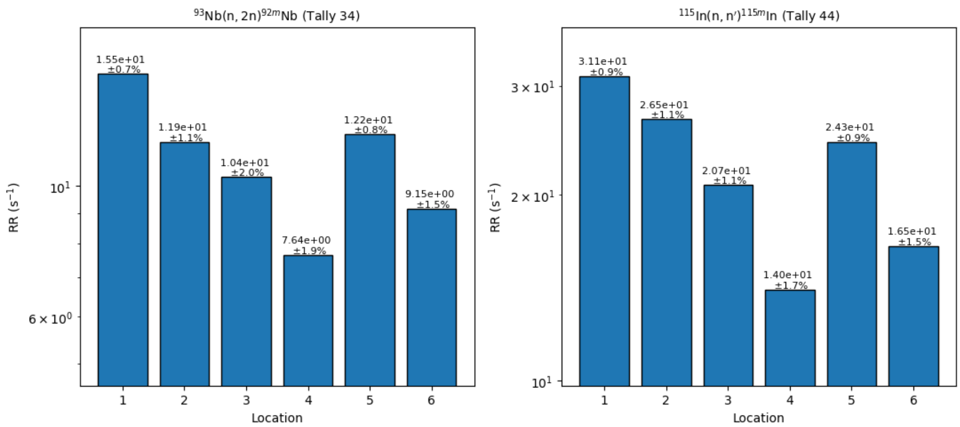

Figure 5.33: Cavity plane $Z = 20$, two-foil stack (Nb, In)

5.4. Photon field

In fusion-relevant environments, photons arise predominantly from neutron-induced reactions such as inelastic scattering, radiative capture and activation processes. These secondary gamma fields contribute significantly to the total dose absorbed by structural materials and electronic components, as will be shown in section 5.4.

From a radiation damage perspective, photons play a different but non-negligible role compared to neutrons: while the latter are responsible for atomic displacements and material embrittlement, photons primarily deposit energy by interacting with the target's electrons, inducing ionization. This is especially relevant for semiconductor-based electronics and diagnostic instrumentation, where total ionizing dose effects can lead to performance degradation and long-term reliability issues [51] [52].
Therefore, although the GENeuSIS project isn't focused on reproducing the photon energy spectra, the characterization of the photon field inside the GENeuSIS cavity is important in order to understand the overall radiation environment where components may be exposed.

5.4.1. Mesh tallies

The mesh parameters are the same from simulations with neutrons, which means that they cover the whole 30x30x30 cm cavity and have voxel sizes of 1x1x1 cm. Results show a quite different behaviour with respect to the neutron spatial distribution, since the photons seem to have a flatter and more uniform profile that decreases perpendicularly as the Y axis progresses. This is in contrast with the neutrons more spherical wavefront. The point of highest flux is different from the one of the neutrons, being 3 cm higher on the Z-axis (Z=-4) but still centred on the X-axis and on the first surface of the cavity Y-axis wise.

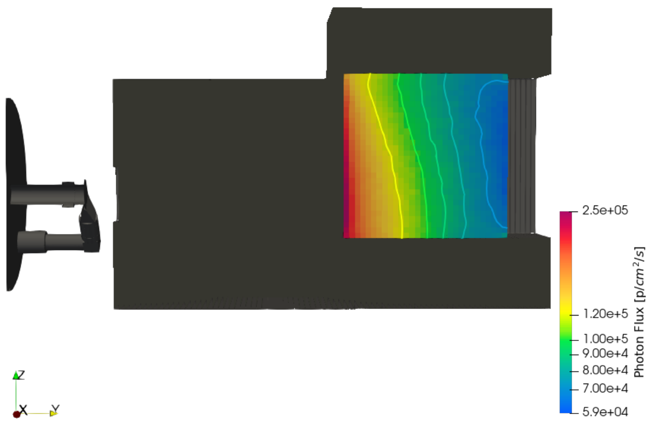

Figure 5.34: Section of the photon spatial distribution along the cavity midplane (X=0), logarithmic scale. The contour lines values are indicated in the legend ($1.2 \times 10^5, 1 \times 10^5, 9 \times 10^4, 8 \times 10^4, 7 \times 10^4$).

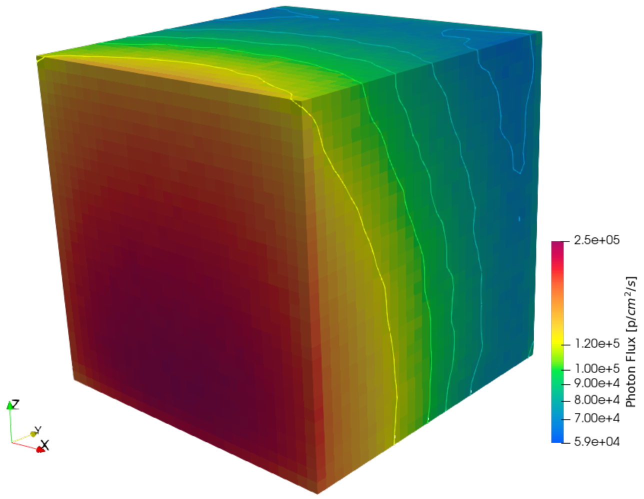

Figure 5.35: Photon spatial distribution of the whole cavity, logarithmic scale. The countour lines values are indicated in the legend $(1.2 \times 10^5, 1 \times 10^5, 9 \times 10^4, 8 \times 10^4, 7 \times 10^4)$.

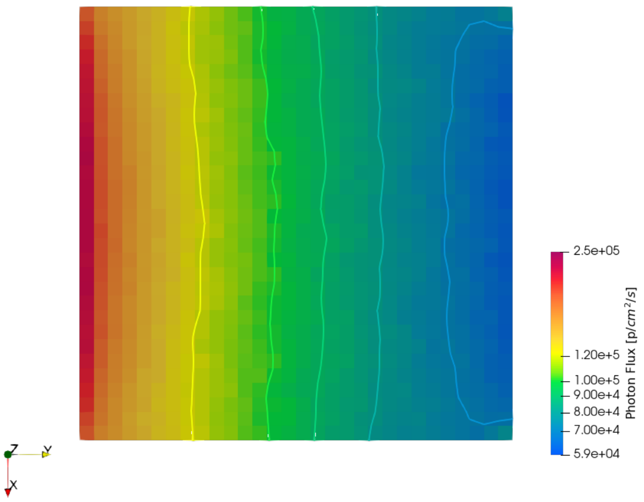

Figure 5.36: The same mesh from figure 5.35 but cut in the middle (Z=8 plane) and viewed from the top, logarithmic. The countour lines values are indicated in the legend $(1.2 \times 10^5, 1 \times 10^5, 9 \times 10^4, 8 \times 10^4, 7 \times 10^4)$.

5.4.2. F5 and cell tallies

The same analysis applied to neutrons was also conducted for photons; for a complete description of the methodology, refer to Section 5.1.2.
The photon distribution follows a similar spatial pattern to that of the neutrons within the cavity, as the flux decreases following a similar trend, although the decline is slightly less steep. Overall, the photon flux is relatively high, approaching the magnitude observed in ITER, which makes it a non-negligible factor in the design and interpretation of future in situ tests.

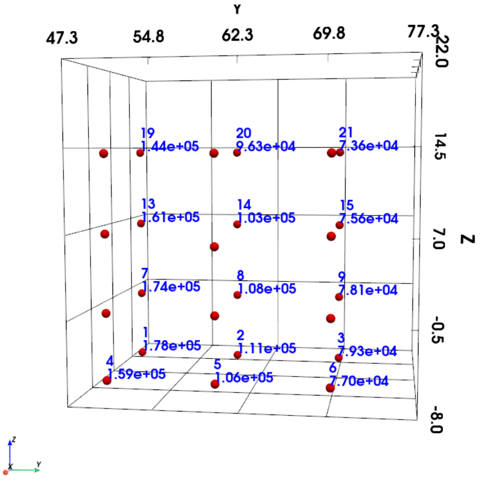

Figure 5.37: F5 tallies along the x=0 plane (and 3 from the x=13 plane). The values are in $n/(\text{cm}^2\,\text{s})$.

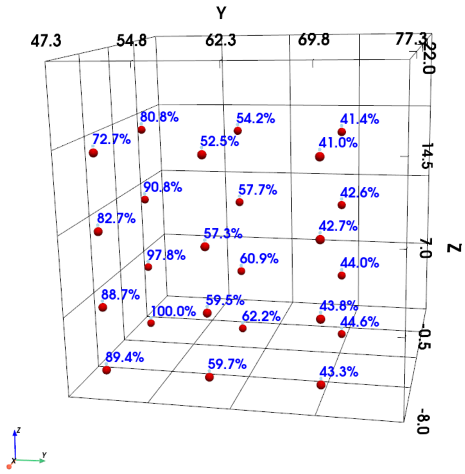

Figure 5.38: Tallies' flux values with respect to the tally 255.

The photon spectra from each F5 tally were compared and found to be nearly identical. This indicates that, although the flux can vary significantly across different regions of the cavity, the energy distribution remains essentially unchanged. The cavity-averaged energy distribution was calculated using 15 energy groups and subsequently compared to the ITER Workstation 5 photon spectrum (Figure 5.39).

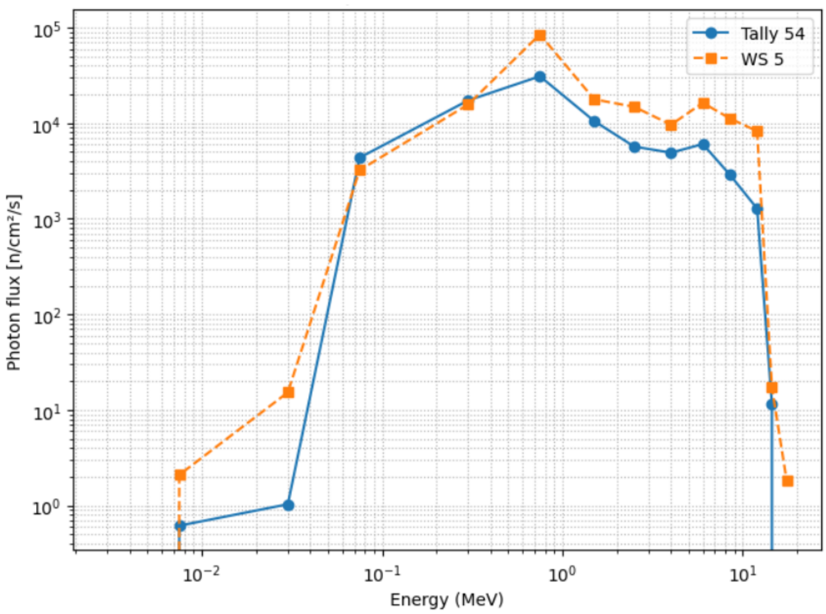

Figure 5.39: Comparison of the photon spectra from the whole GENeuSIS cavity (Tally 54) and the one calculated for the ITER workstation 5.

By using the workstation 5 (WS 5) spectra as a reference it's possible to calculate the usual statistical metrics:

Tally	Pearson r	R_{rel}	R_{mag}
54	0.923	4.5	2.3

Table 5.6: Comparison of Spectral Metrics between the photons of the GENeuSIS cavity and ITER workstation 5.

The high Pearson correlation indicates that the shapes of the two spectra match very well while the R_{mag} indicates that, overall, the ITER spectrum is roughly one order of magnitude higher. These difference in magnitude is to be expected since the two spectra are not normalized, just like the very high R_{rel}.

5.5. Mesh Dose Tallies

In order to estimate the dose electronic components would receive within the GENeuSIS-II irradiation cavity, MCNP mesh tallies were used to generate dose maps for materials such as silicon, copper, and stainless steel. This approach allows for a more general framework, removing the need to model individual components and providing the user with a 3D map that can be quickly consulted.
The results take into account the contributions of both photons and neutrons. In this approach, a regular three-dimensional mesh is superimposed over the region of interest. MCNP then obtains the energy deposition (heating) tally from a track-length estimator applied over the spatial region of interest and convolved with an energy-dependent response function. The tally estimates the average energy deposited per unit mass (MeV/g) through the following formula [53]:

$$H_t \ = \ \frac{\rho_a}{m} \int_V \int_0^\infty \int_{4\pi} \phi(\mathbf{r}, E, \Omega)\, \sigma_t(E)\, H(E)\, \mathrm{d}\Omega\, \mathrm{d}E\, \mathrm{d}V, \tag{5.2}$$

where $\phi(\mathbf{r}, E, \Omega)$ is the particle flux (particles/cm^2/steradian/MeV), $\sigma_t(E)$ is the microscopic total cross section (barn), $H(E)$ is the heating number (MeV/collision), ρ_a is the atomic density $[at/cm^3]$, V is the volume of voxel region (cm^3) and m is the mass of the voxel (g).
To obtain the absorbed dose in Gray per second, the result is then multiplied by the yield and the units are converted from MeV to Joules and from grams to kilos.
The analysis was performed for Stainless Steel (SS), copper and silicon, since these materials are commonly used in the structural components and electronics of fusion devices. The contribution of photons dominates energy deposition compared to neutrons, generally being one order of magnitude higher.
The plots of the dose in copper and stainless steel have the same contour lines values to make any comparison easier.

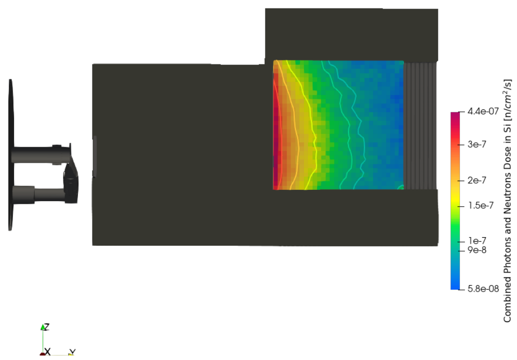

Figure 5.40: The dose calculated in Gy/s for Si, logarithmic. The contour lines values are indicated in the legend $(1 \times 3^{-7}, 2 \times 10^{-7}, 1.5 \times 10^{-7}, 1 \times 10^{-7}, 9 \times 10^{-8})$

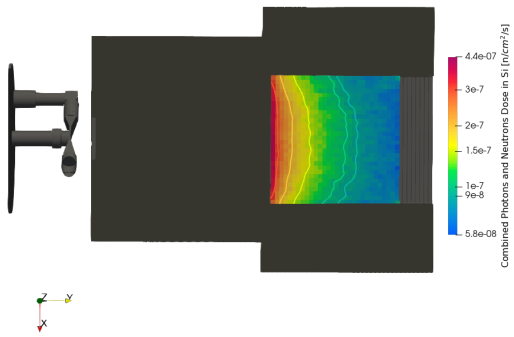

Figure 5.41: The same mesh from figure 5.40 but cut in the middle of the cavity (Z=8 plane), logarithmic. The contour lines values are indicated in the legend $(1 \times 3^{-7}, 2 \times 10^{-7}, 1.5 \times 10^{-7}, 1 \times 10^{-7}, 9 \times 10^{-8})$

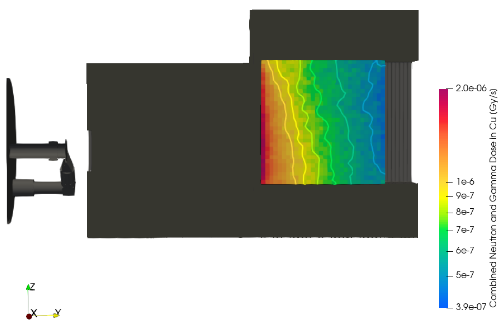

Figure 5.42: The dose calculated in Gy/s for Cu, logarithmic. The contour lines values are indicated in the legend $(1 \times 10^{-6}, 9 \times 10^{-7}, 8 \times 10^{-7}, 7 \times 10^{-7}, 6 \times 10^{-7}, 5 \times 10^{-7})$

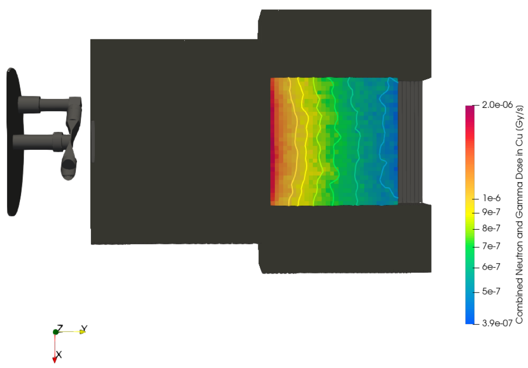

Figure 5.43: The same mesh from figure 5.42 but cut in the middle of the cavity (Z=8 plane), logarithmic. The contour lines values are indicated in the legend $(1 \times 10^{-6}, 9 \times 10^{-7}, 8 \times 10^{-7}, 7 \times 10^{-7}, 6 \times 10^{-7}, 5 \times 10^{-7})$

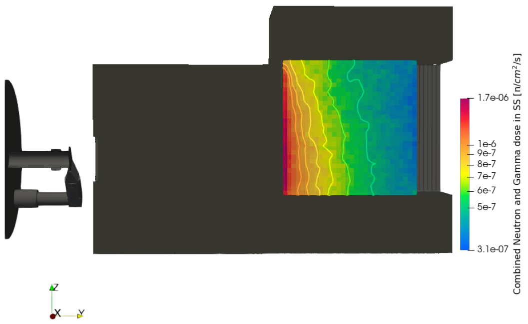

Figure 5.44: The dose calculated in Gy/s for SS, logarithmic. The contour lines values are indicated in the legend ($1\times10^{-6}, 9\times10^{-7}, 8\times10^{-7}, 7\times10^{-7}, 6\times10^{-7}, 5\times10^{-7}$)

Figure 5.45: The same mesh from figure 5.44 but cut in the middle of the cavity (Z=8 plane), logarithmic. The contour lines values are indicated in the legend ($1\times10^{-6}, 9\times10^{-7}, 8\times10^{-7}, 7\times10^{-7}, 6\times10^{-7}, 5\times10^{-7}$)

6 | Conclusions and future developments

Electronics and diagnostic systems intended for operations in fusion Tokamaks require irradiation campaigns performed under accurately controlled and well characterized neutron fields. In this context lies the goal of this thesis: ensuring that the GENeuSIS-II assembly meets the design criteria and that its irradiation cavity is thoroughly characterized both spectrally and spatially.
In order to achieve its goals this thesis has:

- Increased the fidelity of the GENeuSIS model by adding the dedicated structural support system for the assembly, modeling it and integrating it into the MCNP geometry. The inclusion of these structural elements also led to a measurable improvement in spectral agreement with the ITER Port Cell target by increasing by around 10% the total flux in the cavity, mostly by populating the thermal region. The structure will be implemented in the models of future experimental configurations at the Frascati Neutron Generator to improve their fidelity.

- Carried out a complete neutron and photon field characterization through Monte Carlo simulations performed with MCNP. The study quantified flux gradients and spectral variations within the 30×30×30 cm^3 cavity.
  3D maps of the fluxes were first plotted to gain a general understanding of the flux distribution, then the regions of interest's energy spectra were sampled using f5 tallies and thus an an analysis of the spectral deviations from the ITER reference was performed.
  The results demonstrate that, although the cavity is not perfectly isotropic in flux intensity, the spectral shape remains consistent across most of the irradiation volume, with deviations primarily limited to the thermal region. This highlights the reliability of GENeuSIS-II in reproducing the Port Cell radiation environment.
  The cavity's inner surface was then divided into sections to analyse the direction of the particles crossing them, in order to establish the existence of preferential stream-

ing directions. It established that most of the neutrons travel along the front-back direction of the assembly, but the walls of the cavity still contribute significantly (from 5 to 8 times less).

- In view of the upcoming experimental campaigns, comprehensive models of the DIAMON detector and the activation foil system were developed and tested within the cavity. These analyses confirmed that the presence of such instrumentation does not introduce significant perturbations to the neutron field, preserving both flux intensity and spectral shape within negligible margins.

The work therefore establishes a robust computational framework for future irradiation campaigns at FNG.
At the time of writing, the GENeuSIS-II assembly is under procurement and is expected to be assembled in situ in March. The next phase will focus on experimental validation of the predicted neutron and photon fields, including benchmarking the response of DIAMON detectors and activation foils against MCNP predictions. Subsequent irradiation campaigns on SRAMs and other electronic devices under ITER-like Port Cell conditions at FNG will provide experimental data for the evaluation of Single Event Effect (SEE) rates and for the validation of the radiation transport software.
Beyond the specific case of GENeuSIS-II, the methodology developed in this work can be directly integrated into the design and qualification process of future GENeuSIS configurations.

Bibliography

[1] Francesco Romanelli. *Fusion Electricity: a Roadmap to the Realisation of Fusion Energy*. EUROfusion Programme Management Unit, Germany, 2012. ISBN 978-3-00-0407. doi: https://euro-fusion.org/eurofusion/roadmap/.

[2] T. Donné et al. *European Research Roadmap to the Realisation of Fusion Energy*. EUROfusion, November 2018. ISBN 978-3-00-061152-0. URL `https://www.euro-fusion.org`. ISBN 978-3-00-061152-0.

[3] Romanelli, Francesco. Fusion energy. *EPJ Web Conf.*, 246:00013, 2020. doi: 10.1051/epjconf/202024600013. URL `https://doi.org/10.1051/epjconf/202024600013`.

[4] 2025. URL `https://www.iter.org/`.

[5] Pietro Barabaschi et al. Iter progresses into new baseline. *Fusion Engineering and Design*, 215:114990, 2025. doi: 10.1051/epjconf/202024600013. URL `https://doi.org/10.1016/j.fusengdes.2025.114990`.

[6] M. Martone, M. Angelone, and M. Pillon. The 14 mev frascati neutron generator. *Journal of Nuclear Materials*, 212-215:1661–1664, 1994. ISSN 0022-3115. doi: https://doi.org/10.1016/0022-3115(94)91109-6. URL `https://www.sciencedirect.com/science/article/pii/0022311594911096`. Fusion Reactor Materials.

[7] Francis F Chen. *Introduction to Plasma Physics*. Plenum Press, New York, 1974. ISBN 978-0306307775.

[8] Marc Haber, Elia Abdo, and Joseph Younes. A study of the use of a thorium fuel cycle in a molten salt reactor. Master's thesis, American University of Beirut, 2017. URL `https://www.researchgate.net/publication/323116700_A_STUDY_OF_THE_USE_OF_A_THORIUM_FUEL_CYCLE_IN_A_MOLTEN_SALT_REACTOR`. Accessed: 15 Feb 2026.

[9] M.Kikuchi, K.Lackner, and M.Q.Tran. Fusion physics. 2012.

[10] Fabio Moro. *3-D nuclear analyses for the design of plasma neutron and gamma diagnostic systems in the ITER tokamak Equatorial Port 1*. Phd thesis, University of

Rome Tor Vergata, Rome, Italy, 2012–2013. Work performed in collaboration with ENEA (Frascati) and F4E.

[11] Yidong Wu. *Fusion Neutronics*. Springer Singapore, Singapore, 2017. ISBN 978-981-10-4490-8. doi: 10.1007/978-981-10-4491-5.

[12] M. Angelone, M. Pillon, and R. Villari. Feasibility of irdff validation by benchmark/mock-up experiments performed at the 14 mev frascati neutron generator. Frascati, via E. Fermi, 45 00044 Frascati (Italy), 2013.

[13] Clément Lemaignan. Nuclear materials and irradiation effects. In Dan Gabriel Cacuci, editor, *Handbook of Nuclear Engineering*, pages 565–635. Springer, Boston, MA, 2010. ISBN 978-0-387-98149-9. doi: 10.1007/978-0-387-98149-9_6.

[14] K. H. Beckurts and K. Wirtz. *Neutron Physics*. Springer Berlin, Heidelberg, 1964. ISBN 978-3-642-87616-5. URL `https://doi.org/10.1007/978-3-642-87614-1`.

[15] Paul Reuss. *Neutron Physics*. EDP Sciences, 2008. ISBN 978-2-7598-0041-4.

[16] Sarah L. Harris and David Harris. 3 - sequential logic design. In Sarah L. Harris and David Harris, editors, *Digital Design and Computer Architecture*, pages 106–169. Morgan Kaufmann, 2022. ISBN 978-0-12-820064-3. doi: https://doi.org/10.1016/B978-0-12-820064-3.00003-9. URL `https://www.sciencedirect.com/science/article/pii/B9780128200643000039`.

[17] Ygor Quadros de Aguiar, Frédéric Wrobel, Jean-Luc Autran, and Rubén García Alía. *Introduction to Single-Event Effects*, pages 29–47. Springer International Publishing, Cham, 2025. ISBN 978-3-031-71723-9. doi: 10.1007/978-3-031-71723-9_2. URL `https://doi.org/10.1007/978-3-031-71723-9_2`.

[18] Mitsuru Kikuchi, Karl Lackner, and Minh Quang Tran. *FUSION PHYSICS*. IAEA Library Cataloguing in Publication Data, 2012. ISBN 978–92–0–130410–0. URL `https://www.iaea.org/publications/8879/fusion-physics`.

[19] P.N. Yushmanov, T. Takizuka, K.S. Riedel, O.J.W.F. Kardaun, J.G. Cordey, S.M. Kaye, and D.E. Post. Scalings for tokamak energy confinement. *Nuclear Fusion*, 30 (10):1999, oct 1990. doi: 10.1088/0029-5515/30/10/001. URL `https://doi.org/10.1088/0029-5515/30/10/001`.

[20] R. Andreani, M. Dalle Donne, G. Muro, L. Plöchl, and M. R. N. Simon. Overview of the european union fusion nuclear technologies development and essential elements on the way to demo. *Fusion Engineering and Design*, 81(1-7):25–32, 2006.

doi: https://doi.org/10.1016/j.fusengdes.2005.09.005. Proceedings of the 8th International Symposium on Fusion Nuclear Technology.

[21] L. A. Artsimovich. Tokamak devices. *Nuclear Fusion*, 12(2):215–252, 1972. doi: 10.1088/0029-5515/12/2/012.

[22] Yu. Utin, K. Ioki, A. Alekseev, Ch. Bachmann, S. Cho, V. Chuyanov, L. Jones, E. Kuzmin, M. Morimoto, M. Nakahira, and G. Sannazzaro. Design progress of the iter vacuum vessel sectors and port structures. *Fusion Engineering and Design*, 82(15):2040–2046, 2007. ISSN 0920-3796. doi: https://doi.org/10.1016/j.fusengdes.2007.07.009. URL `https://www.sciencedirect.com/science/article/pii/S0920379607003547`. Proceedings of the 24th Symposium on Fusion Technology.

[23] Esposito Basilio et al. Progress of design and development for the iter radial neutron camera. *J Fusion Energ*, 41:22, 2022. URL `https://doi.org/10.1007/s10894-022-00333-9`.

[24] Domenico Marzullo et al. Mechanical design of iter radial neutron camera ex-port system. *Fusion Engineering and Design*, 203:114477, 2024. URL `https://doi.org/10.1016/j.fusengdes.2024.114477`.

[25] Yunbo Zhai, G. Loesser, M. Smith, Wenping Wang, V. Udintsev, Thibaud Giacomin, Andrei Khodak, David Johnson, and Russell Feder. Multiphysics engineering analysis for iter diagnostic first wall and shield module design*. *Energy and Environmental Engineering*, 3:67–81, 11 2015. doi: 10.13189/eee.2015.030401.

[26] Marta Damiano. Neutronics study for the design of geneusis: a neutron test bed facility for diagnostics and critical components of iter. Master's thesis, Università di Trento, 2022/2023.

[27] V.S. Udintsev, P. Maquet, E. Alexandrov, N. Casal, D. Cuenca, J.-M. Drevon, R. Feder, J.P. Friconneau, T. Giacomin, J. Guirao, S. Iglesias, F. Josseaume, B. Levesy, D. Loesser, J. Ordieres, E. Quinn, S. Pak, C. Penot, C.S. Pitcher, M. Portalès, M. Proust, A. Suarez, F. Seyvet, V. Tanchuk, Y. Utin, C. Vacas, C. Vasseur, and M.J. Walsh. Final design of the generic equatorial port plug structure for iter diagnostic systems. *Fusion Engineering and Design*, 96-97:993–997, 2015. ISSN 0920-3796. doi: https://doi.org/10.1016/j.fusengdes.2015.05.021. URL `https://www.sciencedirect.com/science/article/pii/S0920379615003191`. Proceedings of the 28th Symposium On Fusion Technology (SOFT-28).

[28] J.M. Drevon et al. Process and overview of diagnostics integration in iter ports.

Fusion Engineering and Design, 88(2):1306–1309, 2013. doi: https://doi.org/10.1016/j.fusengdes.2013.02.059.

[29] Göran Ericsson. Advanced neutron spectroscopy in fusion research. *Journal of Fusion Energy*, 38, 2019. doi: 10.1007/s10894-019-00213-9. URL `https://doi.org/10.1007/s10894-019-00213-9`.

[30] E.E. Lewis and W. F. Miller Jr. *Computational Methods of Neutron Transport*. A WILEY-INTERSCIENCE PUBLICATION - JOHN WILEY SONS, USA, 1984. ISBN 0-471-09245-2.

[31] Monographs. *Neutronics*. CEA Saclay and Groupe Moniteur (Éditions du Moniteur), France, 2015. ISBN 978-2-281-11372-3.

[32] Alberto Previti. *Fast and Accurate Numerical Solutions in Some Problems of Particle and Radiation Transport: Synthetic Acceleration for the Method of Short Characteristics, Doppler-broadened Scattering Kernel, Remote Sensing of the Cryosphere*. PhD thesis, Università di Bologna, Bologna, Italy, 2014. URL `https://amsdottorato.unibo.it/id/eprint/6599/`. Doctoral Thesis in Energy Engineering and Innovation.

[33] Dan Gabriel Cacuci. *Handbook of Nuclear Engineering*. Springer Science, 2010. ISBN 978-0-387-98130-7.

[34] MCNPX-5 Monte Carlo Team. *MCNP – A General Monte Carlo N-particle transport code overview and theory (Version 5, vol. I)*. Los Alamos National Laboratory, Los Alamos, NM, 2003. URL `https://mcnp.lanl.gov/`.

[35] F. Iannone. Cresco enea hpc clusters: a working example of a multifabric gpfs spectrum scale layout. *Proceedings of the 2019 International Conference on High Performance Computing Simulation (HPCS)*, pages 1051 – 1052, 2019. doi: https://doi.org/10.1109/HPCS48598.2019.9188135.

[36] Joel A. Kulesza, Terry R. Adams, Jerawan Chudoung Armstrong, Simon R. Bolding, Forrest B. Brown, Jeffrey S. Bull, Timothy Patrick Burke, Alexander Rich Clark, III Forster, Robert Arthur, Jesse Frank Giron, Tristan Sumner Grieve, Colin James Josey, Roger L. Martz, Gregg W. McKinney, Eric John Pearson, Michael Evan Rising, Jr. Solomon, Clell Jeffrey, Sriram Swaminarayan, Travis John Trahan, Stephen Christian Wilson, and Anthony J. Zukaitis. *MCNP®: Theory & User Manual, Code Version 6.3.0*. Los Alamos National Laboratory, Los Alamos, NM, 2022. URL `https://mcnp.lanl.gov/`.

[37] 2026. URL `https://www.ornl.gov/division/rnsd/projects/automated-variance-reduction-generator-advantg-software`.

[38] E. J. McGrath and D. C. Irving. *Techniques for efficient Monte Carlo Simulation - Vol III Variance Reduction*. Oak Ridge National Laboratory (ORNL) - Radiation Shielding Information Center (RSIC), 1975.

[39] J. S. Hendricks and T. E. Booth. Mcnp variance reduction overview. *Monte-Carlo Methods and Applications in Neutronics, Photonics and Statistical Physics. Lecture Notes in Physics*, 240, 2006. doi: https://doi.org/10.1007/BFb0049037.

[40] 2026. URL `https://nds.iaea.org/fendl/`.

[41] G. Schnabel, D. L. Aldama, T. Bohm, U. Fischer, S. Kunieda, A. Trkov, C. Konno, R. Capote, A. J. Koning, S. Breidokaite, T. Eade, M. Fabbri, D. Flammini, L. Isolan, I. Kodeli, M. Kostal, S. Kwon, D. Laghi, D. Leichtle, S. Nakayama, M. Ohta, L. W. Packer, Y. Qiu, S. Sato, M. Sawan, M. Schulc, G. Stankunas, M. Sumini, A. Valentine, R. Villari, and A Zohar. Fendl: A library for fusion research and applications. *Nuclear Data Sheets*, pages 1–78, 2024. doi: 10.1016/j.nds.2024.01.001.

[42] M. Damiano, R. Villari, A. Colangeli, D. Flammini, N. Fonnesu, P. Gaudio, M. Lungaroni, F. Moro, S. Noce, A. Previti, and R. Rossi. Preliminary study for a machine learning model for geneusis. *Fusion Engineering and Design*, 224:115594, 2026. ISSN 0920-3796. doi: https://doi.org/10.1016/j.fusengdes.2025.115594. URL `https://www.sciencedirect.com/science/article/pii/S0920379625007896`.

[43] D. Flammini, A. Chaudhary, A. Colangeli, N. Fonnesu, J. Guirao, K. Gupta, S. Kalwale, G. Mariano, F. Moro, A. Previti, M. Quatrevaux, P. Shigin, V.S. Udintsev, and R. Villari. Neutronic analyses for the equatorial diagnostic port plug 12 in iter. *Fusion Engineering and Design*, 193:113639, 2023. ISSN 0920-3796. doi: https://doi.org/10.1016/j.fusengdes.2023.113639. URL `https://www.sciencedirect.com/science/article/pii/S0920379623002223`.

[44] 2025. URL `https://www.oecd-nea.org/tools/abstract/detail/NEA-1703/`.

[45] 2025. URL `https://www.paraview.org/`.

[46] 2025. URL `https://fispact.ukaea.uk/wiki/CCFE-709_group_structure`.

[47] Andrea Pola, Dario Rastelli, Matteo Treccani, Stefano Pasquato, and Davide Bortot. Diamon: A portable, real-time and direction-aware neutron spectrometer for field characterization and dosimetry. *Nuclear Instruments and Methods in Physics Research Section A: Accelerators, Spectrometers, Detectors and Associ-*

ated Equipment, 969:164078, 2020. ISSN 0168-9002. doi: https://doi.org/10.1016/j.nima.2020.164078. URL `https://www.sciencedirect.com/science/article/pii/S0168900220305027`.

[48] Saverio Braccini, Pierluigi Casolaro, Gaia Dellepiane, Isidre Mateu, Lorenzo Mercolli, Andrea Pola, Dario Rastelli, and Paola Scampoli. A novel experimental approach to characterize neutron fields at high- and low-energy particle accelerators. *Scientific Reports*, 12, 2022. URL `https://doi.org/10.1038/s41598-022-21113-7`.

[49] IAEA Nuclear Data Section. Exfor experimental nuclear reaction database. `https://nds.iaea.org/exfor/servlet/E4sMakeE4`. Accessed: 2026-02-14.

[50] D. Flammini, F. Andreoli, M. Angelone, S. Cesaroni, A. Colangeli, M. Damiano, N. Fonnesu, S. Loreti, M. Lungaroni, F. Moro, S. Noce, G. Pagano, A. Pensa, A. Pietropaolo, M. Pillon, A. Previti, and R. Villari. Tungsten benchmark shielding experiment at the frascati neutron generator. In *Proceedings of the 20XX International Conference on Fusion Energy (SOFT 2025)*.

[51] Luca Reali, Mark R. Gilbert, Max Boleininger, and Sergei L. Dudarev. -photons and high-energy electrons produced by neutron irradiation in nuclear materials. *Journal of Nuclear Materials*, 585:154584, 2023. ISSN 0022-3115. doi: https://doi.org/10.1016/j.jnucmat.2023.154584. URL `https://www.sciencedirect.com/science/article/pii/S0022311523003513`.

[52] Ali Khoshnoud and Javad Yavandhassani. Modeling of total ionizing dose (tid) effects on the nonuniform distribution of si/sio2 interface trap energy states in mos devices. *Scientific Reports*, 15(1):17082, 2025. ISSN 2045-2322. doi: 10.1038/s41598-025-01325-3. URL `https://doi.org/10.1038/s41598-025-01325-3`.

[53] J. E. Sweezy, T. E. Booth, F. B. Brown, J. S. Bull, J. S. Casswell, L. J. Cox, J. T. Durkee, J. S. Elson, M. L. Fensin, R. A. Forster, J. T. Goorley, J. S. Hendricks, H. G. Hughes, M. R. James, R. C. Johns, R. C. Little, R. L. Martz, G. W. McKinney, D. E. Post, R. E. Prael, A. J. Rendell, T. D. Rice, H. R. Trellue, L. S. Waters, M. C. White, T. Wilcox, and A. J. Zukaitis. MCNP – A General Monte Carlo N-Particle Transport Code, Version 5 – Volume I: Overview and Theory. Technical Report LA-UR-03-1987, Los Alamos National Laboratory, Los Alamos, NM, 2008. URL `https://mcnp.lanl.gov/pdf_files/la-ur-03-1987.pdf`. Revised 2/1/2008.

[54] OECD Nuclear Energy Agency. JANIS: JAva-based Nuclear Data Information System Web Interface, 2026. URL `https://www.oecd-nea.org/janis`. Accessed: March 2, 2026.

A | Appendix A

A.1. Formulas

Pearson Correlation

$$r = \frac{\sum_{i=1}^{N}\left(\phi_i^{\mathrm{GEN}} - \langle\phi^{\mathrm{GEN}}\rangle\right)\left(\phi_i^{\mathrm{ITER}} - \langle\phi^{\mathrm{ITER}}\rangle\right)}{\sqrt{\sum_{i=1}^{N}\left(\phi_i^{\mathrm{GEN}} - \langle\phi^{\mathrm{GEN}}\rangle\right)^2 \sum_{i=1}^{N}\left(\phi_i^{\mathrm{ITER}} - \langle\phi^{\mathrm{ITER}}\rangle\right)^2}} \tag{A.1}$$

where ϕ_i^{GEN} and ϕ_i^{ITER} are the neutron flux values in the i-th energy group for, respectively, the GENeuSIS and the ITER reference spectra and N is the total number of energy groups. The quantities $\langle\phi^{\mathrm{GEN}}\rangle$ and $\langle\phi^{\mathrm{ITER}}\rangle$ represent the mean spectral values averaged over all energy groups.

Root Mean Square Ratio

$$R_{mag} = \frac{\sqrt{\frac{1}{N}\sum_{i=1}^{N}\left(\phi_i^{\mathrm{GEN}}\right)^2}}{\sqrt{\frac{1}{N}\sum_{i=1}^{N}\left(\phi_i^{\mathrm{ITER}}\right)^2}} \tag{A.2}$$

where ϕ_i^{GEN} and ϕ_i^{ITER} denote the neutron flux values in the i-th energy group of the GENeuSIS and ITER reference spectra, respectively, and N is the total number of energy groups.

Root Mean Square Relative Difference

$$R_{rel} = \sqrt{\frac{1}{N}\sum_{i=1}^{N}\left(\frac{\phi_i^{\mathrm{GEN}} - \phi_i^{\mathrm{ITER}}}{\phi_i^{\mathrm{ITER}}}\right)^2} \tag{A.3}$$

A.2. OpenMC

OpenMC is a modern, open-source Monte Carlo particle transport code developed primarily for neutron and photon transport applications. Unlike MCNP, OpenMC adopts a fully object oriented architecture and is designed to integrate with high-level scripting languages, most notably Python. This approach allows the user to build the geometry, run a simulation and process the data all in one jupyter notebook, significantly streamlining the process. To tests its accuracy compared to MCNP the GENeuSIS geometry was exported to OpenMC. The only issue is that the OpenMC neutron source that reproduces FNG's radial and energy distribution is currently under development.
For this reason the model was tested using a point source and a spherical source. The same setup was reproduced with MCNP in order to have a good comparison.
Note that a 1cm spherical source emitting 14 MeV neutrons isotropically is a decent approximation of FNG, since simulations ran with MCNP with the sphere and the FNG source achieved a Pearson correlation of 0.9958 and an average difference of 6.5 % (in the cavity, which is relatively far from the source). The point source achieved similar results, with a Pearson r of 0.9956 and and an average difference of 7.6%.
The simulations for OpenMC were ran on a Ryzen 9 cpu with 16 cores (5 GHz clock rate) using 10^9 particle histories, taking around 15 minutes, while for MCNP they were executed on ENEA's CRESCO HPC using 192 cpus and taking around 1 hour.
The results, for this application, are certainly impressive since the two mesh from figure A.1 and A.2 both have a similar Pearson r of 0.995 and an average difference of 2.5%, which is to be attributed to statistical noise since without weight windows or an extreme amount of particle histories the errors on each voxel are around 1%.

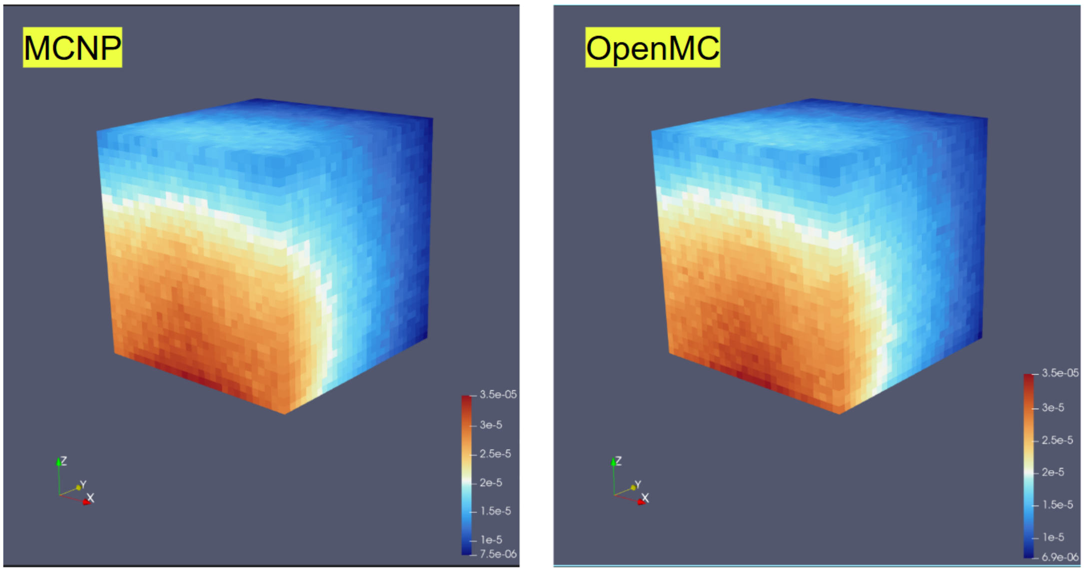

Figure A.1: Meshes of the neutron flux of the cavity for the point source. The values are in $n/(\mathrm{cm}^2\,\mathrm{s})$

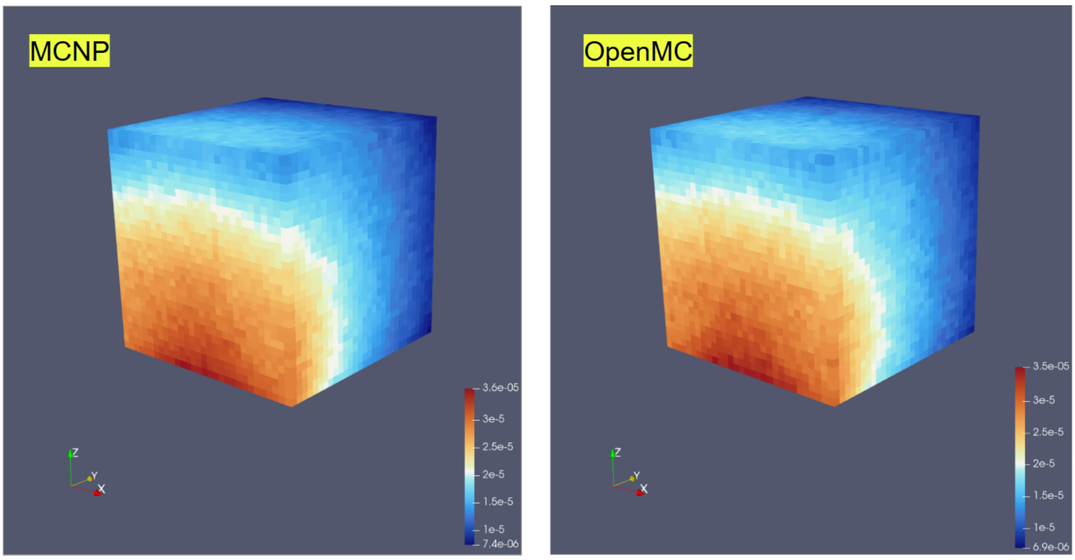

Figure A.2: Meshes of the neutron flux of the cavity for the spherical source. The values are in $n/(\mathrm{cm}^2\,\mathrm{s})$

A.3. Cross sections of the foils reactions

The following cross sections plots have been taken from the NEA official website [54].

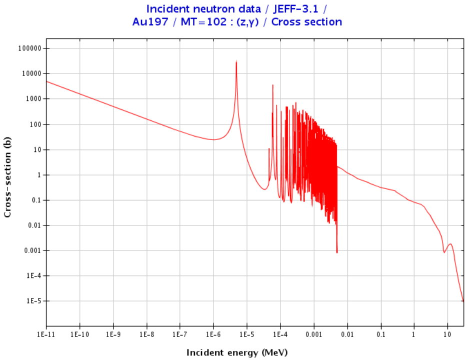

Figure A.3

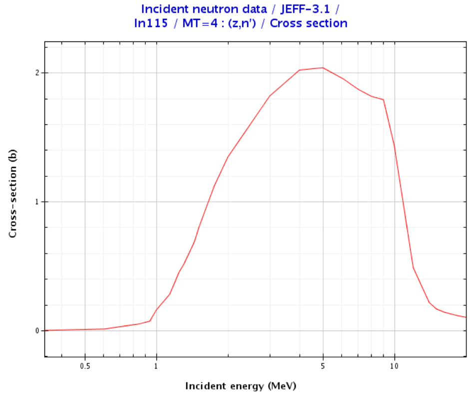

Figure A.4

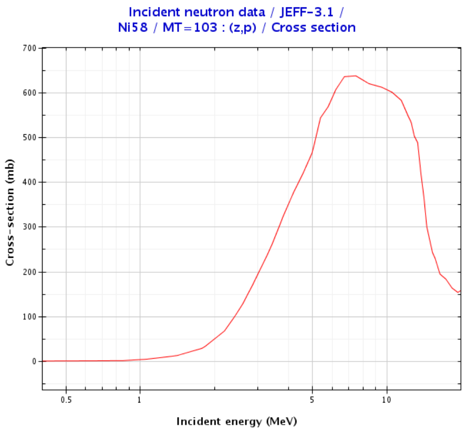

Figure A.5

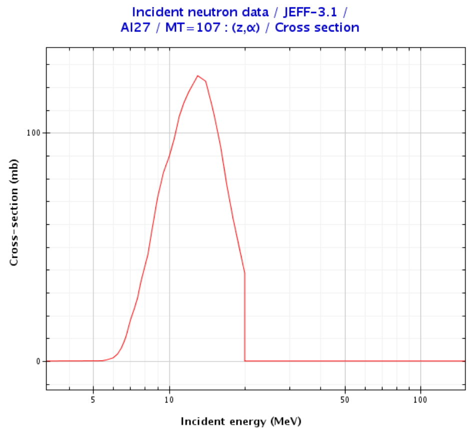

Figure A.6

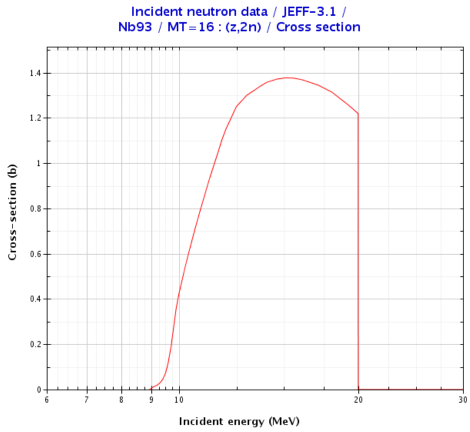

Figure A.7

A.4. F5 tallies with x=0 and x=7

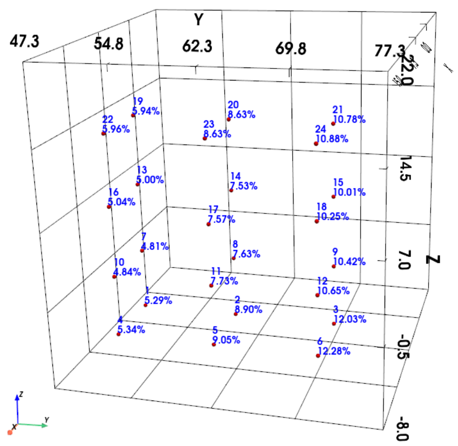

Figure A.8: How much of each f5 tally spectrum is comprised by neutrons with energy lower than 10^{-6}MeV.

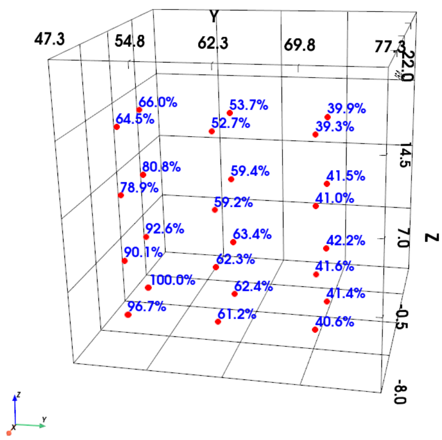

Figure A.9: Tallies' flux values with respect to tally 1.

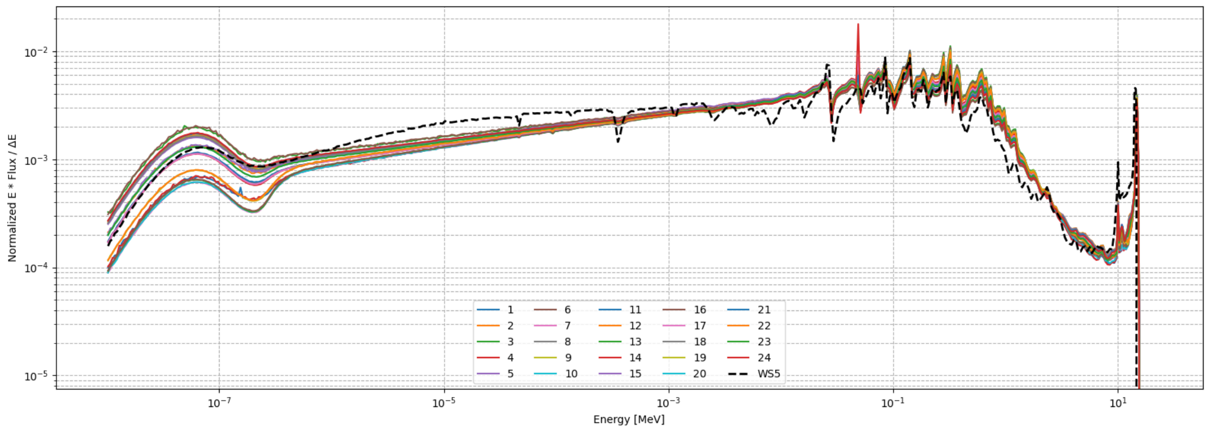

Figure A.10: Spectra inside the cavity, calculated by means of F5 tallies.

Tally	Pearson r	R_{rel}	Mean % Diff
1	0.88282	0.428	36.796
2	0.90199	0.299	23.396
3	0.90262	0.347	26.678
4	0.88484	0.422	36.395
5	0.90059	0.298	23.303
6	0.90140	0.353	26.992
7	0.87307	0.461	39.096
8	0.89098	0.352	28.181
9	0.89953	0.329	26.345
10	0.87648	0.454	38.806
11	0.89177	0.346	27.859
12	0.89955	0.329	26.303
13	0.87167	0.455	38.415
14	0.88781	0.360	28.915
15	0.89643	0.332	26.875
16	0.87517	0.447	38.002
17	0.88637	0.356	28.682
18	0.89744	0.329	26.521
19	0.88165	0.403	33.568
20	0.89590	0.323	25.753
21	0.89981	0.331	26.338
22	0.88448	0.397	33.236
23	0.89590	0.323	25.753
24	0.83611	0.352	26.529

Table A.1: Comparison of normalized spectra against the WS5 reference spectrum.

List of Figures

List of Tables

Acknowledgements

I would like to express my gratitude to Professor Andrea Pola for his supervision and for providing the opportunity to carry out this thesis work.
A special thank goes to my supervisors and all of the great friends I made at ENEA, as their help and availability at all times proved invaluable. Simone, Fabio, Andrea, Marta, Rosaria, Samuele, Roberto, Virginie, Silvia, Nicola, Nicholas, Michele, JF, Davide and Villie all have a special place in my heart and made my stay at ENEA very enjoyable, especially when delicious pastries were involved.